Materials Characterization 240 (2026) 116733

Contents lists available at ScienceDirect

Materials Characterization

journal homepage: www.elsevier.com/locate/matchar

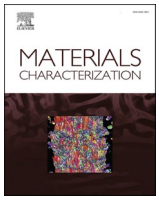

Characterization of the substructure around grain boundaries in a hot-deformed Ni-30%Fe austenite model alloy

Pablo Garcia-Chao [a,*], Winfried Kranendonk [b], Cornelis Bos [a,b], Jilt Sietsma [a], Sven Erik Offerman [a]

[a] Department of Materials Science and Engineering, Delft University of Technology, Mekelweg 2, 2628 CD Delft, the Netherlands
[b] Tata Steel Nederland, P.O.Box 10000, 1970 CA IJmuiden, the Netherlands

ARTICLE INFO

Keywords:
Subgrains
Grain boundaries
Austenite
Electron backscatter diffraction
Dislocation density

ABSTRACT

The nucleation of recrystallization is determined by the properties of the underlying subgrains: namely, subgrain size and misorientation. Under defined conditions, recrystallization nucleation occurs at the boundaries between deformed grains, and their junctions. Nevertheless, previous characterization studies have dedicated no specific attention to the subgrains located around deformed grain boundaries. In this view, the substructure at such locations is here characterized for a hot-deformed Ni-30%Fe austenite alloy, employing electron backscatter diffraction. Firstly, results show that the boundary length fraction not surrounded by subgrains decreases with higher dislocation density around the boundary. Higher boundary dislocation density also results in smaller subgrain sizes and higher subgrain misorientations. The subgrain size reduction is appropriately described by a Staker-Holt-type relationship. This is the case despite the spatial gradient and relatively high values of the dislocation densities surrounding the deformed grain boundaries. To describe the increase in subgrain misorientation, a novel equation is proposed, showing good agreement with experimental data. Apart from this, subgrains neighboring triple grain junctions exhibit higher misorientations than those located around the boundaries, away from the junctions. This explains the preferential recrystallization nucleation at triple-junction sites. Finally, unlike suggested in literature, twin boundaries accumulate lower dislocation densities than general high-angle boundaries. This explains their lower recrystallization nucleation efficiencies. Nevertheless, for equal boundary dislocation density, the substructure developed around both boundary types does not differ significantly.

1. Introduction

Metals subjected to plastic deformation often develop subgrain structures (simply referred to as substructures) inside deformed grains. This is particularly the case when deformation is applied at high temperature, and/or when the stacking fault energy (SFE) of the metal is high [1,2]. Subgrains are separated from each other by boundaries with low-angle boundary (LAB) character, i.e., whose misorientations are smaller than a certain threshold (typically, 15° [3]). In general, LABs can be described as dislocation arrays, where the misorientation across the boundary is dictated by the spacing between dislocations [4]. Consequently, the sizes and misorientations of the subgrains are determined by the specific distribution of the dislocations generated by the plastic deformation into subgrain boundaries.

Substructures have been observed to significantly affect the mechanical behavior of deformed metals in many different ways. For instance, they provide work hardening [1,5–10], improve creep strength [11,12], act as preferential sites for fatigue crack initiation and propagation [13–15] or precipitation [16,17], and give rise to abnormal grain growth [18,19]. Furthermore, subgrains present in deformed microstructures are the origin of recrystallization in metals [3,20]. In fact, recrystallization theories directly associate the event of nucleation with the characteristics of the underlying subgrain, namely its size and/or misorientation [21–29]. Accordingly, physics-based models of the nucleation of recrystallization require subgrain properties as input, including subgrain size and misorientation [21–27]. Quantitatively predicting the nucleation of recrystallization has attracted a wealth of research [21–28], because it defines the grain size and texture resulting from the process [3,30–33].

For these reasons, substructures have been characterized in detail for a wide range of metals, after deformation in different conditions

* Corresponding author.
E-mail address: chao.p.g@gmail.com (P. Garcia-Chao).

https://doi.org/10.1016/j.matchar.2026.116733
Received 26 May 2026; Received in revised form 26 June 2026; Accepted 2 July 2026
Available online 6 July 2026

Abbreviations

CI	Confidence index
CSL	Coincidence site lattice
DRX	Dynamic recrystallization
EBSD	Electron backscatter diffraction
FCC	Face-centered cubic
FTB	Former twin boundary
GNB	Geometrically necessary boundary
GND	Geometrically necessary dislocation
GOS	Grain orientation spread
HAB	(General) high-angle boundary
HABx3	Junction of three general high-angle boundaries
HAB-FTB	Junction of two general high-angle boundaries and a former twin boundary
IDB	Incidental dislocation boundary
IPF	Inverse pole figure
KAM	Kernel average misorientation
LAB	Low-angle boundary
MDRX	Metadynamic recrystallization
SIBM	Strain-induced boundary migration
SFE	Stacking fault energy
SRX	Static recrystallization
SSD	Statistically stored dislocation
TEM	Transmission electron microscopy

Symbols

b	Burgers vector length
A_{GB}	Area of the subgrain layer surrounding a deformed grain boundary
$\overline{D}_G$	Average (deformed) grain size
d_{SG}	Diameter of a subgrain
$\overline{d}_{SG}$	Average diameter of the subgrains located around a deformed grain boundary
K_{SH-GB}	Staker-Holt constant (around a deformed grain boundary)
L_{SG}	Length of a subgrain boundary
$\overline{L}_{SG}$	Average length of the subgrain boundaries located around a deformed grain boundary
N_{dis}	Number of dislocation lines making up an individual low-angle boundary
$\overline{N}_{dis}$	Average number of dislocation lines making up the individual subgrain boundaries in the subgrain layer surrounding a deformed grain boundary
N_{dis-GB}	Number of dislocation lines contained in the subgrain layer surrounding a deformed grain boundary
$N_{dis-LAB}$	Total number of dislocation lines contained in all the individual subgrain boundaries within the subgrain layer surrounding a deformed grain boundary
N_{SG}	Number of subgrains in the subgrain layer surrounding a deformed grain boundary
θ_{SG}	Average misorientation across a subgrain boundary
$\overline{\theta}_{SG}$	Average misorientation between the subgrains located in the subgrain layer surrounding a deformed grain boundary and their parent grain
ρ_{GB}	Average dislocation density around a deformed grain boundary

[2,5–7,18,34–40]. Nevertheless, a limitation of these studies is that they have only dealt with the substructure as a whole. In this sense, no specific attention has been paid to the subgrains located around the deformed grain boundaries. However, those subgrains are of the greatest interest to recrystallization: when deformation has been performed at high temperature [23,41–43] or at low temperature up to low or medium strains [21,28,38,44] (i.e., in conditions of relatively low stored energy [3]), the nucleation of recrystallization takes place at the boundaries between the deformed grains, and their junctions. Furthermore, after deformation under those conditions, dislocation densities are much higher around deformed grain boundaries and junctions than in the deformed grain interiors [29,45–47]. Hence, the subgrain sizes and misorientations at those locations are expected to significantly differ from those in the deformed grain interiors. The nucleation of recrystallization at deformed grain boundaries has been related to the effect of strain-induced boundary migration (SIBM), or bulging, of those boundaries [1,21,23,24,27,38,41,48–50]. Particularly, nucleation occurs when the LAB of a subgrain neighboring the deformed grain boundary increases its misorientation so that it transforms into a high-angle boundary (HAB) [29,51]. This imparts high mobility to the nucleus boundary, activating its significant growth into the surrounding deformed microstructure [29,51]. Besides, detailed characterization of the substructure of austenite after hot deformation has been performed for relatively high strains only (i.e., higher than 0.5 [34,35]). These lead to dynamic/metadynamic recrystallization (DRX/MDRX) [27,30,41]. On the other hand, comparable characterization is still to be performed for lower strains (e.g., 0.2 [43,52]), which give rise to static recrystallization (SRX). Lower strains produce lower dislocation densities [3]. As a result, different subgrain sizes and misorientations are expected, compared to the case of higher strains. SRX in austenite is highly relevant in practice for, e.g., the hot rolling of steels. Moreover, it has been the subject of extensive research over the years (e.g., [23,42,43,52–54]).

Apart from this, the development of microstructural models which incorporate the substructure calls for a relationship between subgrain properties and other parameters characterizing the deformed condition. For instance, Staker and Holt proposed a relationship between the average subgrain size and dislocation density in the microstructure, whereby subgrain size is inversely proportional to the square root of dislocation density [37]. This relationship has been shown to hold for different metals and deformation conditions [37,55,56]. Furthermore, it is widely used in practice (e.g., [11,27,56–61]). Even so, past studies testing the Staker-Holt relationship were based on subgrains in deformed grain interiors only [37,55,56], where dislocation densities can be lower than around deformed grain boundaries [29,45–47]. At the same time, other studies have suggested that subgrain sizes can only decrease with higher dislocation density up to a certain dislocation density value [1,5–7,62]. Therefore, whether the relationship by Staker and Holt also holds for the subgrains surrounding deformed grain boundaries is unclear. Additionally, an analogous relationship between subgrain misorientation and dislocation density has not been found in the literature. This can be partly attributed to the later development of reliable techniques which can determine subgrain misorientations, compared to subgrain sizes [5]. However, such an equation is practically required to the same extent as the one concerning the subgrain size. For example, the nucleation of recrystallization is determined by subgrain misorientations: subgrains with higher initial misorientations are more likely to reach first an HAB misorientation [1,29,49,50].

Finally, in the case of SRX nucleation occurring at deformed grain boundaries, marked differences exist regarding the role played by the various types of boundaries and junctions. However, the rationale for those differences is not understood, in terms of the nucleation mechanism. Firstly, triple junctions have often been noted to play a preferential role [52,63,64]. Moreover, for a given deformed grain boundary, new SRX grains tend to appear earlier at the triple junctions than at the other nucleation sites along the boundary (grain-boundary nucleation sites) [43]. Secondly, annealing twin boundaries exhibit much lower

SRX nucleation efficiencies (number of SRX grains produced per unit of boundary length) than general HABs [43]. Distinct dislocation accumulation behavior has been effectively shown for annealing twin boundaries in face-centered cubic (FCC) metals. However, some studies have measured higher dislocation densities compared to general HABs [65–70], while others have found the opposite trend [45]. The trend that effectively applies to each FCC alloy and/or deformation condition is currently not known. Furthermore, whether both boundary types also exhibit different subgrain development properties (and how those may explain the lower SRX nucleation efficiencies of twin boundaries) has not been examined either.

Within this context, this study presents a systematic characterization of the substructure in a Ni-30%Fe austenite alloy, after hot deformation to a relatively low strain (0.2). Emphasis is placed on the subgrains located around the deformed grain boundaries. The specific deformation conditions have been selected in agreement with the industrial practice in hot rolling [43,53,54,71,72]. For this alloy and deformation conditions, the occurrence of SRX as opposed to DRX/MDRX was confirmed in [29]. Moreover, the nucleation of SRX was found to primarily occur at deformed grain boundaries and junctions [43]. As a characterization technique, electron backscatter diffraction (EBSD) has been chosen. EBSD is nowadays the regular technique used for substructure characterization [7,18,34–36,39,52,73]: the spatial and angular resolutions suffice to resolve the vast majority of the subgrains [36], while providing statistical representativity. By contrast, older studies made use of transmission electron microscopy (TEM) [1,5,6,37,38,40,74]. TEM offers finer spatial and angular resolutions than EBSD, but at the expense of much smaller analyzed areas [75]. Additionally, the present study provides the dislocation densities around the deformed grain boundaries, as also measured by EBSD. Physics-based equations are then tested for the relationship between those dislocation densities and the resultant subgrain misorientations and sizes. Throughout the study, particular attention is devoted to the properties of the subgrains surrounding triple grain junctions and annealing twin boundaries, and to the magnitude of the dislocation densities around annealing twin boundaries.

2. Experimental methods

2.1. Material and thermo-mechanical processing

The characterization in this study was performed on an alloy with a Ni-30%Fe (in wt%) chemical composition. The SFE of this alloy is similar to that of the austenite in carbon steels [76]. However, unlike in carbon steels, austenite is the stable phase of Ni-30%Fe both at high and room temperature. This makes it possible to characterize the substructure formed at high temperature. As a result, Ni-30%Fe has been extensively employed as a model for substructure development during hot deformation. This has been done for a range of deformation conditions, albeit different from those considered here, and without paying specific attention to the subgrains surrounding the deformed grain boundaries [34,35,73,77–80].

Specimens from this Ni-30%Fe alloy were subjected to hot uniaxial compression in a Bähr DIL 805 A/D dilatometer. The grain size was ~90 μm. Deformation was applied at a temperature of 900°C, to a strain of 0.2, and with a strain rate of 1 s^{-1}. Such deformation conditions [43,53,54,71,72] and initial grain size [71,78] were selected in line with those typical in the hot rolling of metals. The specimens were quenched immediately after deformation, inside the dilatometer chamber. The time between the end of compression and the start of quenching was ~0.5 s.

Further details about the present alloy and dilatometer experiments are available in [43].

2.2. EBSD characterization of the deformed substructure

Characterization of the deformed substructure in the dilatometer specimens was performed by EBSD. In particular, three areas with a size of at least 170 × 140 μm^2 each were scanned. All were taken near the center of a cross-section normal to the cylindrical axis of the specimen, and at mid-sample length. The measurements were carried out in a Thermo Fisher Helios G4 PFIB UXe dual beam scanning electron microscope, equipped with an Ametek EDAX Hikari Plus EBSD detector, and with APEX 2.5.1 as the acquisition software. The acquisition was performed with an accelerating voltage of 20 kV, a beam current of 6.4 nA, and a working distance of 6 mm. A step size of 50 nm was employed for all the scans, in a hexagonal grid. This step size corresponds to the accepted spatial resolution of the EBSD technique [81]. Overall, the results in this study are based on over 200 deformed grain boundaries and over 15,000 subgrains.

Post-processing of the EBSD maps was carried out with the OIM Analysis v8 package. A neighbor orientation correlation algorithm was applied to eliminate wild spikes. A Kuwahara filter was also used for noise reduction. This filter reduces the noise in the maps while preserving the subgrain boundaries. Five iterations of the filter were applied [82], in accordance with the procedure in [7,36]. Afterwards, deformed grains were constructed as entities bounded by a misorientation of at least 15°, with an internal grain orientation spread (GOS) higher than 1.2°, and minimum size of 10 pixels. The threshold misorientation of 15° was chosen because SRX grains in austenite do not form at deformed grain boundaries with lower misorientations than 15° [43]. The deformed grains resulting from this procedure were then further discretized into subgrains. These were detected with a minimum boundary misorientation of 0.5°, minimum confidence index (CI) of 0.1 [83], and minimum size of 0.25 μm (Fig. 1). Besides, only subgrains with a smaller size than 3.3 μm were included in the analysis. This value was selected because it was the size required to avoid considering other features as subgrains, such as deformation bands inside deformed grains [43]. In addition, some recrystallized grains existed in the analyzed maps. These were identified as entities having a misorientation of at least 5° (excluding twin boundaries from the considered boundaries), lower GOS than 1.2°, and minimum size of 5 pixels. The area fraction corresponding to these recrystallized grains was lower than 1%. Sometimes, the reorientation due to annealing twinning after nucleation led portions of recrystallized grains to be separated from their parent deformed grains by boundaries with smaller misorientations than 15° [29]. To avoid considering those portions as subgrains, they were identified in the maps as entities with lower GOS than 1.2°, neighboring a twin boundary, and surrounded by misorientations smaller than 15°. Twin boundaries in FCC alloys are coincident site lattice (CSL) boundaries with either $\sum 3$ or $\sum 9$ character [41,52,84]. These were detected assuming a tolerance of 3° in both the theoretical misorientations and twin planes (60°⟨111⟩ for $\sum 3$ and 38.9°⟨110⟩ for $\sum 9$ [41,52,84]). The condition was also set that boundary traces in the scan were parallel to those that would result for the theoretical CSL boundary plane, within a tolerance of 8°. Former twin boundaries (FTBs) in the deformed grains were identified as those with at least a portion classified as $\sum 3$ or $\sum 9$ according to the aforementioned criterion, or relatively straight boundaries forming a band inside a deformed grain. The density of geometrically necessary dislocations (GNDs) per pixel was derived applying the method in [85] to the 5th-order neighbors. For this purpose, a length of the Burgers vector of 0.2518 nm [86] and the {111}<110 > slip systems were considered. Kernel average misorientation (KAM) values, which provide another measure of the internal dislocation content of a pixel [81], were also obtained from the 5th-order neighbors. Finally, grain and subgrain sizes were calculated as equivalent circle diameters. Owing to the non-uniform directions of grain boundaries in an EBSD map, this method is more appropriate than linear interception to study subgrains surrounding grain boundaries. Moreover, previous work has demonstrated that equivalent diameters result in more accurate quantification of

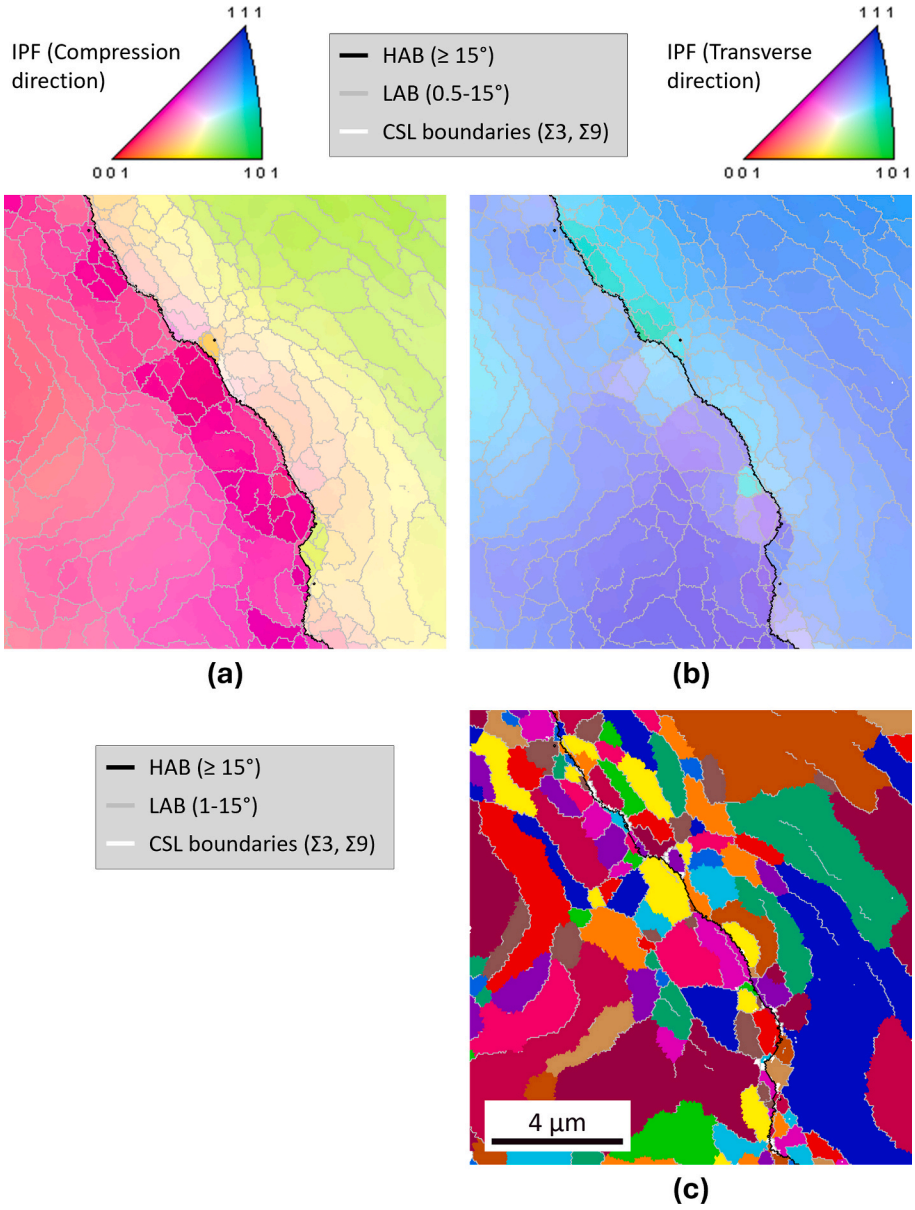

Fig. 1. Example of subgrain detection in a fragment of one of the analyzed EBSD scans: IPF maps (a) parallel and (b) perpendicular to the compression direction, and (c) subgrain map, where each colour represents one of the entities resulting from the deformed grains' discretization into subgrains and parent grains. Black lines indicate boundaries with misorientations higher than 15°, and not identified as CSL boundaries (i.e., general HABs). Gray lines indicate boundaries with misorientations between 0.5 and 15° in (a) and (b), and between 1 and 15° in (c) (i.e., LABs).

subgrain sizes using EBSD than linear interception [36].

The remainder of the analysis was conducted with dedicated Python scripts. Data from the different OIM Analysis partitions were taken as input. The recrystallized grain fragments were excluded from the subgrain analysis comparing the spatial coordinates in the subgrain partition with those in the fragments partition. This procedure was also followed to associate each entity in the subgrain partition to an entity in the deformed grain partition. Within each deformed grain, it was then assumed that the entity with the largest size was the parent grain, and the others were subgrains. The number of deformed grain neighbors of each subgrain was derived from the list of its neighboring entities in the subgrain partition, as determined by OIM. Particularly, that number was taken as the number of different deformed grains associated with the neighboring entities, including its parent grain. Subgrains with three and four deformed grain neighbors are those adjacent to a triple and a quadruple grain junction, respectively. Similarly, subgrains with two deformed grain neighbors are located at grain-boundary sites (i.e., adjacent to a deformed grain boundary, but away from any junction). Finally, subgrains with one deformed grain neighbor are located in a deformed grain interior (i.e., they are not adjacent to any deformed grain boundary).

Subgrain boundary misorientations were calculated as the average of all the pixel-to-pixel misorientations across the boundaries of the subgrain with other entities belonging to the same parent deformed grain. Only misorientations smaller than 15° (the typical threshold for LAB misorientations [3]) were considered for the average. For each subgrain, its boundary pixels were labelled as such after an OIM partition including only the pixels neighboring entity boundaries in the subgrain partition. Boundary GND densities were calculated as the mean GND densities per pixel within layers with approximately 0.5 µm thickness, parallel to a deformed grain boundary, and on either side of it. The pixels inside those layers were selected as those in an additional OIM partition. That partition included only pixels located at a distance of 12 pixels or smaller from any boundary in the deformed grain partition. In this

paper, a deformed grain boundary is thus understood as each layer on either side of a boundary between deformed grains. To ensure the statistical representativity of results, only boundaries with detected lengths larger than 3.75 μm are included in the results provided. For each deformed grain boundary, its subgrain-free length fraction was calculated as the ratio between the number of boundary pixels not belonging to entities labelled as subgrains, and its total number of boundary pixels. Therefore, only entities fully enclosed by LABs did not contribute to the subgrain-free boundary length fractions. The lengths of the deformed grain boundaries were derived as the product of their number of boundary pixels and the map step size.

In all the presented maps, the compression direction is aligned with the horizontal direction of paper. The acquisition and post-processing of the additional EBSD maps, captured with a step size of 0.5 μm, is described in [43].

The uncertainties provided for subgrain sizes and misorientations correspond to standard errors considering the number of analyzed subgrains in each case. The uncertainties given for boundary GND densities and subgrain-free length boundary fractions are standard errors considering the number of analyzed boundaries in each case. The slopes of the linear fits were derived with the specific method in the SciPy library of Python. The indicated uncertainties for those slopes account for a 95% confidence interval.

3. Results and discussion

3.1. Boundary dislocation densities

One representative example of the deformed grains in the analyzed microstructure is displayed in Fig. 2(a), where its boundary segments have been labelled as either general HABs or former twin boundaries (FTBs). Annealing twin boundaries in FCC alloys are CSL boundaries with either ∑3 or, to a lesser extent, ∑9 character [41,52,84]. Yet, the two annealing twin boundaries shown in this grain (both labelled as FTB) had lost their CSL character along their whole lengths due to the plastic deformation (the boundaries are fully drawn as a black line). The twin boundaries in the upper right corner of the image (white arrows in Fig. 2(a)), which belong to a different parent grain, had also lost this CSL character, albeit only along a part of their lengths (the boundaries are drawn partly as a black line, and partly as a white line). This CSL character loss of twin boundaries via plastic deformation, along either their whole or a part of their lengths, has been recurrently reported in past studies on hot-deformed austenite [41,84]. Hence, in the context of deformed microstructures, annealing twin boundaries have been referred to as FTBs [43,84]. In this case, all the annealing twin boundaries present before deformation had lost their CSL character owing to the deformation, totally or partially. Additionally, the triple junctions shown around the same deformed grain have also been labelled according to their type (Fig. 2(a)): junctions of an FTB with the general HAB of the parent grain (HAB-FTB junctions), and junctions between two general HAB segments of the parent grain and the general HAB of a neighboring deformed grain (HABx3 junctions). In this microstructure, the highest dislocation densities are located around deformed grain boundaries and junctions [29] (Fig. 3(a)-(b)). Furthermore, dislocation densities are higher around triple junctions than around the intersecting boundaries, far from the junctions [43]. Specifically, the average GND densities around the triple junctions and grain boundaries of this microstructure were measured in [29] to be higher than the average GND density across the microstructure by factors of ~2.8 and ~2.3 (see Fig. 3(a)-(b), with those GND densities measured within distances of 1 μm around grain boundaries and triple junctions, respectively [29]).

The measured boundary GND density distributions for the general HABs and FTBs in the present microstructure can be seen in Fig. 3(c). FTBs mainly exhibited lower GND densities than general HABs.

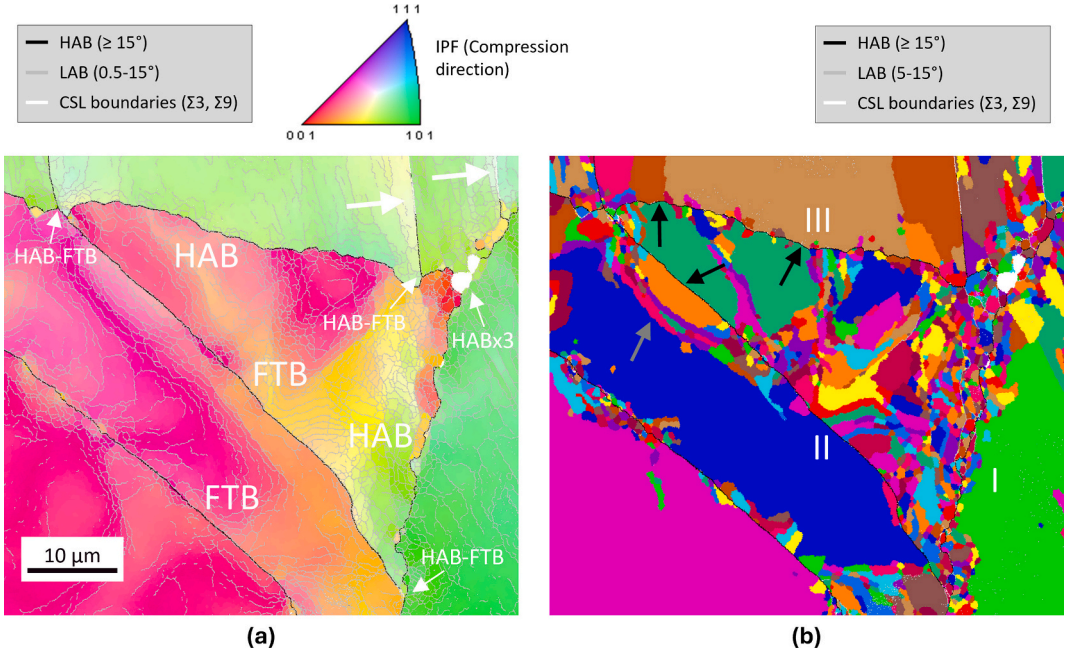

Fig. 2. Fragment of one of the EBSD scans analyzed, representing a portion of a parent deformed grain (partly replotted after [29]): (a) IPF map parallel to the compression direction, and (b) subgrain map, where each colour represents one of the entities resulting from the deformed grains' discretization into subgrains and parent grains. The solid white region corresponds to a recrystallized grain. White lines indicate boundaries detected as Σ3 and Σ9 CSL boundaries (i.e., twin boundaries). Black lines indicate boundaries with misorientations higher than 15°, and not identified as CSL boundaries (i.e., general HABs or former twin boundaries, FTBs). Gray lines indicate boundaries with misorientations between 0.5 and 15° in (a), and between 5 and 15° in (b) (i.e., LABs). The boundary type of each boundary segment of the displayed parent deformed grain has been labelled in (a). The triple junctions corresponding to those boundary segments have also been labelled as HABx3 (junction of three general boundaries) or HAB-FTB (junction of a general HAB and an FTB). The white arrows in (a) point at FTBs within another, adjacent parent deformed grain. The black arrows in (b) highlight subgrain-free regions around the deformed grain boundaries II and III. The gray arrow in (b) denotes an example of elongated features, indicating the micro-bands present in the material.

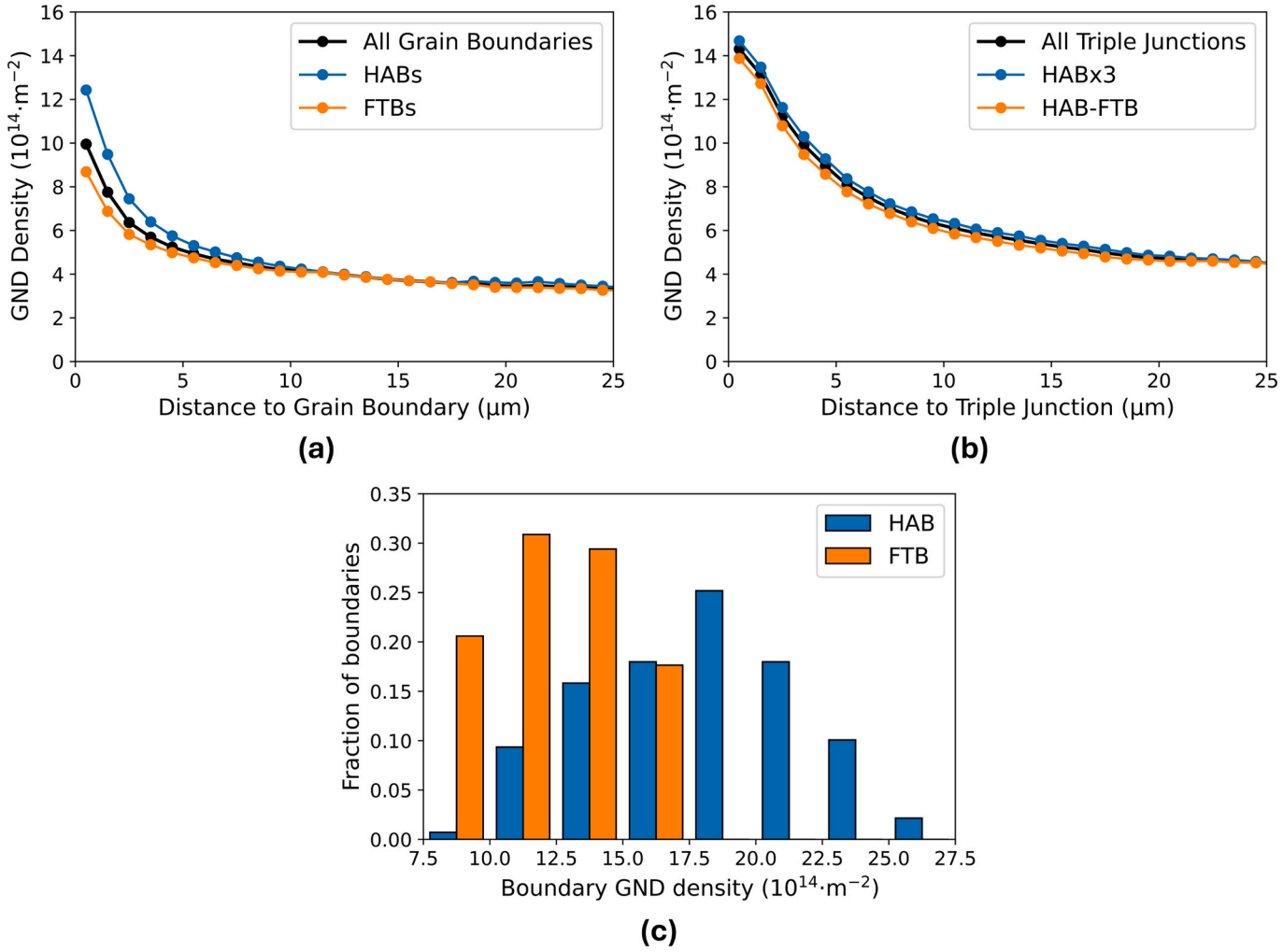

Fig. 3. GND density as a function of the distance to the closest (a) grain boundary and (b) triple grain junction, as analyzed in [29] for the same microstructure of the present study (EBSD step size = 0.5 μm). The black lines give the GND density as a function of the distance to the closest (a) grain boundary or (b) triple grain junction of any type. The blue lines represent the GND density as a function of the distance to the closest (a) general high-angle boundary (HAB) or (b) junction of three general HABs (HABx3 junction). The orange lines represent the GND density as a function of the distance to the closest (a) former twin boundary (FTB) or (b) junction of two general HABs and an FTB (HAB-FTB junction). (c) Distribution of the boundary GND densities for the general HABs and FTBs as measured in this work (EBSD step size = 0.05 μm). (For interpretation of the references to colour in this figure legend, the reader is referred to the web version of this article.)

Although the minimum values were at approximately the same level for both types of boundaries (~$7{\cdot}10^{14}$ m^{-2} for FTBs and ~ $9{\cdot}10^{14}$ m^{-2} for general HABs), the range of GND densities extended to much higher values for general HABs (maximum GND densities of ~$2.6{\cdot}10^{15}$ m^{-2} for general HABs and ~$1.7{\cdot}10^{15}$ m^{-2} for FTBs). Accordingly, the mean boundary GND density was significantly higher around general HABs: ~$1.8{\cdot}10^{15}$ m^{-2}, against ~$1.2{\cdot}10^{15}$ m^{-2} for FTBs (Table 1).

This weaker tendency for dislocation accumulation around FTBs compared to general HABs may appear surprising: recent research on the fatigue behavior of nickel-based superalloys has consistently found the strongest strain localizations to precisely arise around $\sum 3$ twin boundaries [65–68]. By contrast, in this case, general HABs invariably account for the highest GND densities (Fig. 3(c)). That behavior of nickel superalloys has been reported using the same measurement method as in the present study (i.e., GND density as quantified by EBSD) [69]. Moreover, it has also been observed after monotonic loading instead of fatigue [70]. Consequently, neither the cyclic character of the fatigue loads nor the measurement method can explain the different behavior. Nevertheless, recent studies have identified two requirements for this localization of strain near $\sum 3$ boundaries [70,87], which are not fulfilled in the present case. The first is concomitant precipitation

Table 1
Mean boundary GND density, subgrain diameter and subgrain misorientation corresponding to all the general high-angle boundaries (HAB) and former twin boundaries (FTB) analyzed. The subgrain properties correspond to the subgrains located at grain-boundary nucleation sites. The number of boundaries and subgrains examined of each type is also displayed, together with the overall values corresponding to all the boundaries. The uncertainties indicated are the standard errors considering the number of boundaries and subgrains analyzed, respectively.

Type of boundary	HAB	FTB	Total
No. of boundaries analyzed	139	68	207
Boundary length analyzed (mm)	3.60	4.31	7.91
Mean boundary GND density (m^{-2})	1.79 ± 0.03·10^{15}	1.21 ± 0.03·10^{15}	1.60 ± 0.03·10^{15}
Mean subgrain-free boundary length fraction	0.24 ± 0.02	0.33 ± 0.03	0.25 ± 0.02
No. of subgrains analyzed	2680	1761	4441
Mean subgrain diameter (μm)	0.68 ± 0.01	0.78 ± 0.01	0.72 ± 0.01
Mean subgrain misorientation (°)	2.34 ± 0.03	1.92 ± 0.04	2.17 ± 0.02

hardening, which confines the strain to relatively small volumes. The second are low macroscopic strains: in the elastic regime, or just above. In the case dealt with here, Ni-30%Fe is a single-phase alloy with no precipitates. Likewise, the applied strain (i.e., 0.2) is well beyond the macroscopic yield strength. In addition, the strong strain localizations around twin boundaries arise only for certain combinations of slip systems on each boundary side [65,70]. By contrast, other combinations promote dislocation transmission across the boundary. This is because of the good atomic match of the crystals on both sides of the twin boundary, which does not happen at general HABs [65,70]. The present results indicate that, in this case, the behavior of twin boundaries is dislocation transmission (at least, relative to general HABs). Furthermore, these results resemble those reported by Wright *et al.* [45]. Those authors measured considerably lower KAM values around twin boundaries than around general HABs in pure copper deformed at room temperature [45]. This similarity with the study by Wright *et al.* implies that the transmissive behavior of annealing twin boundaries can be generalized to single-phase FCC alloys and strains well beyond the yield strength, applied at both relatively low and high temperatures.

Fig. 4 examines the correlation between the individual boundary GND densities measured and two geometric variables: the length of the boundary and the size of the parent deformed grain, as captured in the EBSD maps. The boundary GND densities of general HABs show a clear decrease with increasing boundary length: relatively short boundaries exhibit both relatively high and low GND densities, while the GND densities of relatively long boundaries are always towards the lower side (blue dots in Fig. 4(a)). This leads to a slope of the linear fit between boundary GND density and boundary length which is significantly different from zero: $(-0.04 \pm 0.03)\cdot10^{14}$ m^{-2}/μm. A linear fit slope that significantly differs from zero implies correlation between the variables. By contrast, the boundary GND densities of FTBs exhibit a much weaker dependence on boundary length (orange dots in Fig. 4(a)). Accordingly, the slope of the linear fit is not significantly different from zero: $(+0.006 \pm 0.013)\cdot10^{14}$ m^{-2}/μm. This suggests a lack of correlation between the variables.

To explain the decreasing trend with increasing boundary length for general HABs, one possibility is that boundary GND densities are reduced with larger size of the parent deformed grain: boundary segments of larger grains can be relatively long or short, depending on where the triple junctions intersect the grain boundary; by contrast, boundary segments of smaller grains can only be relatively short. Moreover, lower average GND densities across the entire grain have typically been reported for larger grain size within a single microstructure [46,47,88]. However, Fig. 4(b) displays that boundary GND densities do not depend on the captured size of the parent deformed grain, neither for general HABs nor for FTBs. This results in linear fit slopes which are not significantly different from zero for either type of boundary: $(-0.02 \pm 0.03)\cdot10^{14}$ m^{-2}/μm and $(-0.01 \pm 0.03)\cdot10^{14}$ m^{-2}/μm, respectively. Another possibility to account for the correlation between boundary GND density and boundary length is the higher GND densities around triple junctions, compared to the areas around the boundaries located away from the junctions (see Fig. 3(a)-(b) and the explanation earlier in this section). In fact, in this case, higher GND densities occur around triple junctions within distances of about 10 μm [29] (e.g., Fig. 3(b)). For shorter boundaries, the areas with locally higher GND density around the junctions will constitute higher fractions of their lengths. In turn, this will lead to a higher measured average GND density along the boundary (i.e., a higher boundary GND density), as effectively observed. The weaker correlation for FTBs can be partly explained by the lower dislocation accumulation around their junctions (HAB-FTB junctions), compared to junctions including general HABs only (HABx3 junctions). Nevertheless, the difference between both junction types is relatively small, with the corresponding dislocation accumulation factors reported as ~2.7 and ~2.9 for HAB-FTB and HABx3 junctions, respectively [29] (Fig. 3(b)). These factors account for the ratio between the average GND density measured within distances of 1 μm around junctions of each type, and the average GND density measured in the entire microstructure [29]. At the same time, FTBs reach larger lengths than general HABs (Fig. 4(a)). For the largest lengths, the areas with increased GND density around the junctions only constitute a negligible fraction of the boundary length. This means that, whereas boundary GND densities monotonically decrease with length for shorter boundaries (e.g., blue line in Fig. 4(a)), they gradually become independent as length increases. That is the behavior exhibited in Fig. 4(a) by FTBs (orange line), and by FTBs and general HABs when considered together (black line).

Finally, the present study does not include the dislocations that EBSD cannot resolve. The spatial resolution of EBSD is restricted to ~0.05 μm [81] (the step size used in the present work). That is insufficient to detect the orientation gradients due to some of the dislocations, which would require a smaller observation volume [89,90]. The dislocations that cannot be detected within a specific observation volume are referred to

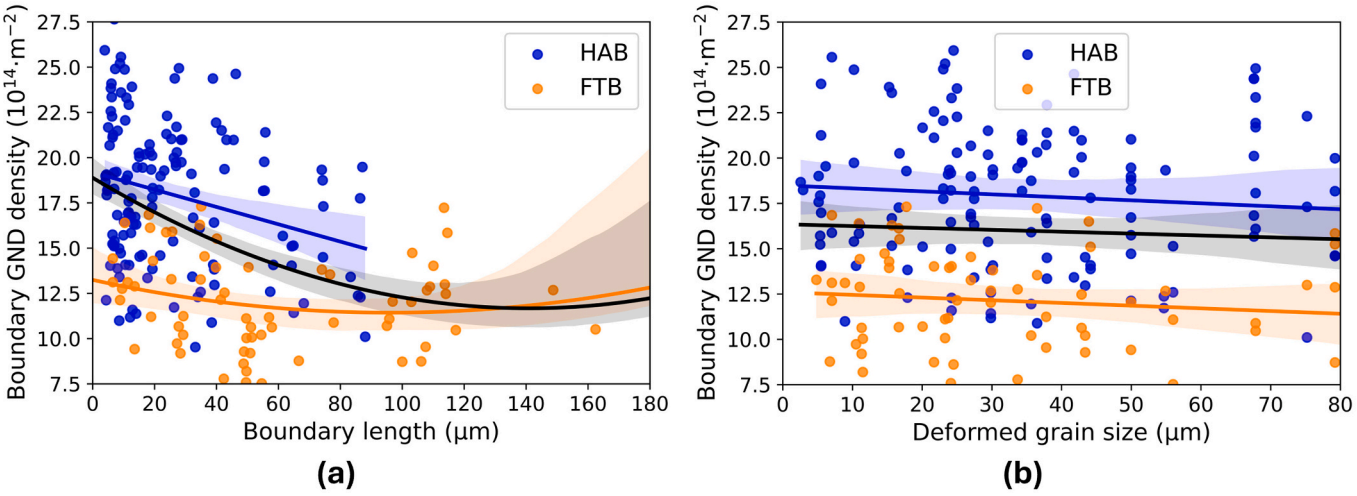

Fig. 4. Boundary GND density as a function of (a) the length of the boundary, and (b) the size of the parent deformed grain. The solid lines in (a) and (b) account for polynomial (order two) and linear regression fits, respectively, and have been added for visual guidance only. The shaded surrounding areas represent a confidence interval for the fits, with a confidence index of 95%. Blue markers and lines correspond to general high-angle boundaries (HAB), and orange ones to former twin boundaries (FTB). The black line displays the combined effect of general HABs and FTBs. (For interpretation of the references to colour in this figure legend, the reader is referred to the web version of this article.)

as statistically stored dislocations (SSDs) [89,90]. By contrast, those that can be detected are geometrically necessary dislocations (GNDs) [89,90]. In this case, the average boundary dislocation density was measured to be $1.48 \pm 0.03 \cdot 10^{15}$ m^{-2} with the current EBSD maps, considering layers of 1 μm around the deformed grain boundaries. With maps having a step size of 0.5 μm (i.e., an order of magnitude coarser), the average boundary dislocation density within the same layer thickness is $1.186 \pm 0.007 \cdot 10^{15}$ m^{-2} [29]. This represents an increase of merely 26% for the step size of 0.05 μm. At the same time, the dislocation density detected by EBSD is known to linearly increase with smaller step size [89,90]. This is the case up to a certain step size, below which the measured dislocation density asymptotically increases towards the total, practically existing dislocation density as the step size approaches zero [89]. Consequently, the fraction of the total dislocation density that is not resolved by EBSD maps with a step size of 0.05 μm will not exceed one ninth of the difference with maps having a step size of 0.5 μm. For the present case, this means that the density of the SSDs cannot exceed, at most, ~3% of the reported dislocation densities. In any case, although the SSDs may have a quantitative effect on the total dislocation density, they do not essentially affect the conclusions of this study. Furthermore, those conclusions mainly involve the GNDs, which are the dislocations that determine the subgrain sizes and misorientations.

3.2. General description of the substructure

The outcome of the substructure analysis performed in this study can be seen for a representative deformed grain in Fig. 2(b). The boundaries of that grain have been labelled as I, II and III. As illustrated by the figure, subgrains were detected both in the deformed grain interiors and around deformed grain boundaries (black lines in the figure). However, relatively large areas also existed in deformed grain interiors, not occupied by any subgrains. Such subgrain-free areas frequently extended to the deformed grain boundaries (e.g., black arrows in the figure). Nevertheless, subgrains were more often found close to the boundaries than in grain interiors. For instance, subgrains exist around a significant portion of the boundary labelled as II, but do not in the neighboring deformed grain interior (entity colored in dark blue). The relatively low density of subgrains in deformed grain interiors is also demonstrated by Table 2, which provides the number of subgrains detected in this study at different types of sites. Particularly, less than 75% of all the subgrains were found not to be adjacent to any deformed grain boundary (i.e., they only had one neighboring deformed grain).

The existence of these subgrain-free regions can be understood considering the TEM analysis in [52], and that subgrains are entities fully surrounded by LABs (with a fraction of such boundaries being HABs instead of LABs, for the subgrains adjacent to deformed grain boundaries). That TEM analysis was performed for the same alloy as studied here, and after very similar deformation conditions [52]. The TEM analysis revealed that the substructure in the deformed grain interiors is formed by micro-bands, bounded by LABs parallel to each other [52]. In that substructure, LABs normal to micro-band boundaries were sometimes found [52]. When these are present, a volume becomes completely surrounded by LABs, effectively leading to a subgrain. However, such perpendicular LABs did not always exist [52]. Accordingly, traces of micro-band boundaries were often detected in deformed grain interiors in the EBSD maps examined here, without associated perpendicular boundaries (see, e.g., the elongated entities highlighted by a gray arrow in Fig. 2(b)). Therefore, the absence of the perpendicular LABs can explain the subgrain-free regions found in the present case.

Table 2
Mean subgrain diameter and misorientation as a function of the number of deformed grains neighboring the subgrain (1 – grain interior, 2 – grain boundary, 3 – triple junction, 4 – quadruple junction). The number of subgrains analyzed of each type is also given, together with the overall values corresponding to all the subgrains. The uncertainties indicated are the standard errors considering the number of subgrains analyzed.

No. of neighboring deformed grains	1	2	3	4	Total
No. of subgrains analyzed	12,315	4441	141	9	16,906
Mean subgrain diameter (μm)	0.91 ± 0.01	0.72 ± 0.01	0.72 ± 0.05	0.55 ± 0.06	0.86 ± 0.01
Mean subgrain misorientation (°)	2.36 ± 0.02	2.17 ± 0.02	3.55 ± 0.18	5.0 ± 1.4	2.33 ± 0.02

Nevertheless, the occurrence of such subgrain-free regions contrasts with most previous studies on substructure characterization. These found grain interiors to be mainly filled by subgrains [7,34–39]. Yet, those studies analyzed lower deformation temperature and/or higher applied strain than here, both of which lead to higher dislocation densities after deformation [3]. Such higher dislocation densities accelerate the dislocation arrangement mechanisms (recovery) enabling subgrain boundary formation [3,79]. This role of a higher dislocation density is confirmed by the TEM analysis in [73]. That analysis was also performed for the alloy employed here and under the same conditions as in [52], except for a significantly higher applied strain (i.e., 0.5). Comparison between the TEM analyses in [52,73] showed that LABs perpendicular to the micro-band boundaries were more profuse for the higher applied strain. Hence, the existence of subgrain-free regions in the case here analyzed can be ascribed to the low applied strain, and subsequently limited dislocation accumulation. Besides, the fact that subgrains were more frequently detected here around deformed grain boundaries than in deformed grain interiors is also due to the higher dislocation densities measured around the boundaries (Fig. 3(a) and Section 3.1). This led to more profuse formation of LABs normal to the micro-band boundaries in those regions (thus mimicking the effect of a higher applied strain as in [73]). Finally, if the material is subjected to further recovery via, e.g., annealing after deformation (i.e., static recovery), subgrains may still develop in the regions here classified as subgrain-free. By these means, the dislocations present in the material can be arranged into normal LABs to the micro-band boundaries. Yet, studying the effects of further annealing is outside the scope of the present study, which focuses on the as-deformed state only.

As explained above, significant regions adjacent to deformed grain boundaries were not occupied by any subgrains (i.e., by regions fully enclosed by LABs, Fig. 2(b)). Nevertheless, considerable differences existed among deformed grain boundaries, in terms of their subgrain-free boundary length fractions. For instance, the boundary segments labelled as II and III in Fig. 2(b) were surrounded by significant subgrain-free areas (subgrain-free length fractions of 0.28 and 0.18, respectively). By contrast, boundary I was essentially fully surrounded by subgrains (subgrain-free length fraction lower than 0.02). This was the case even if all the three boundary segments belonged to the same parent deformed grain. To clarify the reason for these differences, the subgrain-free boundary length fractions of all the analyzed boundaries are plotted against their boundary GND densities in Fig. 5(a). The figure displays that those fractions monotonically decreased with increasing boundary GND density, until reaching a relative saturation for the highest GND densities. Hence, it can be concluded that insufficient dislocation accumulation, and the resultant delay of recovery [3,79], is the reason for the subgrain-free areas around deformed grain boundaries. Specifically, for each boundary, subgrains will exist around the regions with locally higher dislocation densities. By contrast, the areas with locally lower dislocation accumulation will be subgrain-free. For a lower average dislocation density around the boundary, the boundary length fraction corresponding to regions with relatively low dislocation densities will increase. This will, in turn, give rise to a higher subgrain-free boundary length fraction.

The distributions of the subgrain-free boundary length fractions for general HABs and FTBs are plotted separately in Fig. 5(b). The figure shows that the two boundary types followed markedly different

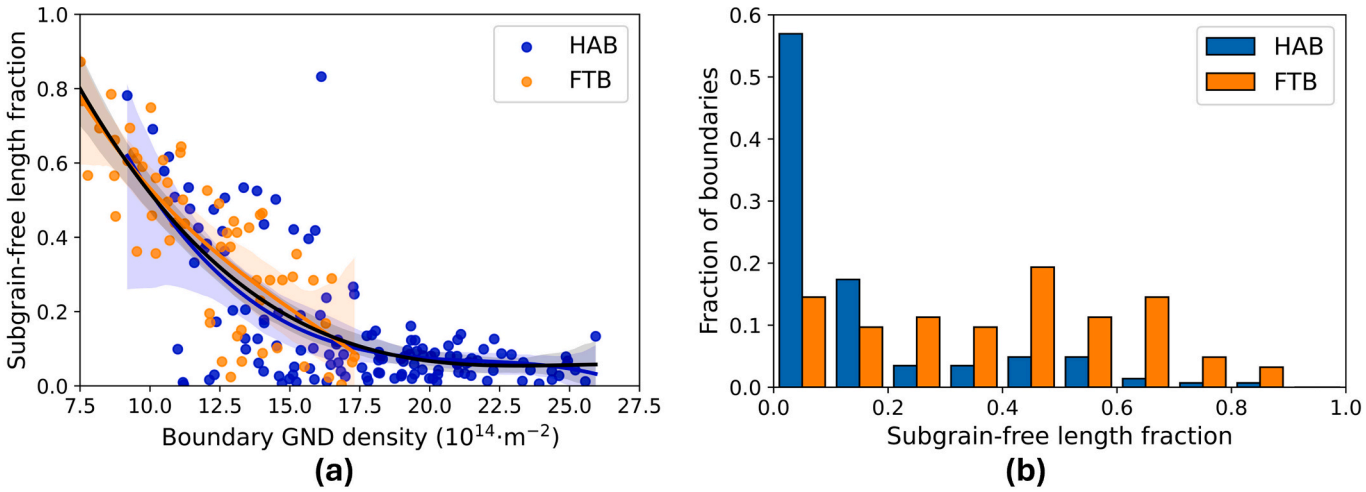

Fig. 5. (a) Fraction of the boundary length that is not surrounded by subgrains (subgrain-free length fraction) as a function of the boundary GND density. (b) Distribution of the subgrain-free length fractions corresponding to general boundaries (HAB) and former twin boundaries (FTB). The solid lines in (a) account for polynomial regression fits (order equal to three), and have been added for visual guidance only. The shaded surrounding areas represent a confidence interval for the fits, with a confidence index of 95%. Blue markers and lines correspond to general high-angle boundaries (HAB), and orange ones to former twin boundaries (FTB). The black line displays the combined effect of general HABs and FTBs. (For interpretation of the references to colour in this figure legend, the reader is referred to the web version of this article.)

distributions. Although both distributions overlapped across most of the entire range between 0 and 1, the distribution for general HABs was centered around the bin with the lowest fractions (0–0.1), whereas that for FTBs was centered around 0.4–0.5. Therefore, FTBs tended to exhibit higher subgrain-free length fractions than general HABs (average fraction of ~0.3 for FTBs against ~0.2 for general HABs, see Table 1). Nevertheless, Fig. 5(a) suggests also that the higher subgrain-free length fractions for FTBs can be solely explained by their lower associated dislocation densities: for the same boundary GND density, their subgrain-free length fractions (orange line in Fig. 5(a)) do not differ

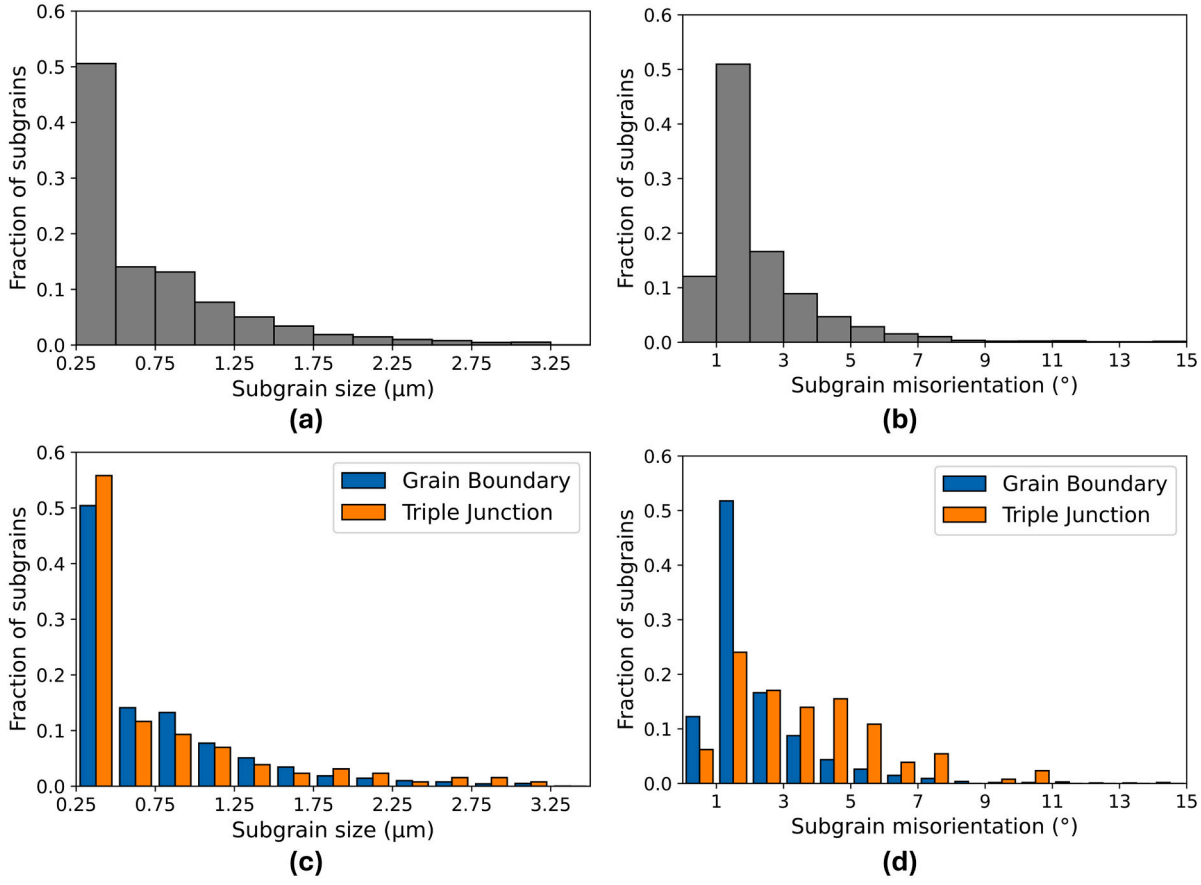

Fig. 6. Distribution of (a, c) the size and (b, d) the misorientation of the subgrains captured, including (a, b) all the subgrains lying around deformed grain boundaries, and (c, d) subgrains lying at grain-boundary and triple-junction sites separately.

significantly from those exhibited by general HABs (blue line in Fig. 5 (a)). This ability of GND densities to essentially determine the subgrain-free length fraction differences between FTBs and general HABs is further illustrated by Fig. 2(b). The boundaries labelled as II (an FTB) and III (a general HAB) showed similar boundary GND densities ($\sim 1.4 \cdot 10^{15}$ m^{-2}), in line with their similar subgrain-free length fractions (~0.2–0.3). Conversely, the boundary GND density of I (a general HAB), whose subgrain-free length fraction was much lower (i.e., lower than 0.02), was considerably higher ($\sim 1.9 \cdot 10^{15}$ m^{-2}). This example also highlights the reason for different subgrain-free length fractions in boundary segments belonging to the same deformed grain: the varying levels of dislocation density accumulated around them.

3.3. Subgrain sizes and misorientations

In this section, the sizes and misorientations of the subgrains located around deformed grain boundaries are examined. This means that subgrains having at least two different neighboring deformed grains, including their parent, are considered (Table 2). The distributions of the sizes and misorientations of these subgrains are shown in Fig. 6(a)-(b). Both seem compatible with lognormal or Rayleigh distributions. This was also the case in previous studies, where subgrain size [2,36,40] and misorientation [2,36,38,74] distributions were reported for all the subgrains in a microstructure, and not only for those located at deformed grain boundaries. The distribution of subgrain sizes is centered around 0.25–0.5 μm (Fig. 6(a)), the bin with the smallest sizes. The subgrain misorientation distribution is centered around 1–2° (Fig. 6(b)).

3.3.1. The relationship with boundary dislocation density

In this subsection, the relationship between boundary dislocation density and the subgrain sizes and misorientations present around the boundary is analyzed. To this end, only subgrains located at grain-boundary sites are considered (i.e., subgrains with exactly two neighboring deformed grains). The relationship between the average subgrain size around a deformed grain boundary and the boundary GND density is first examined in Fig. 7(a). The figure suggests a decrease of the subgrain size with higher boundary GND density. Accordingly, the slope of the linear fit between both variables is equal to $(-0.025 \pm 0.005) \cdot 10^{-14}$ μm/m^{-2} (i.e., significantly different from zero). Similarly, the largest subgrain size around a boundary also decreases with higher dislocation density around the boundary (Fig. 7(c)). The slope of the corresponding linear fit is $(-0.069 \pm 0.019) \cdot 10^{-14}$ μm/m^{-2} (also significantly different from zero). On the other hand, the average subgrain misorientation around a boundary increases with higher boundary GND density (Fig. 7(b)). Fig. 7(d) shows that this is also the case for the largest subgrain misorientation around the boundary. The linear fit

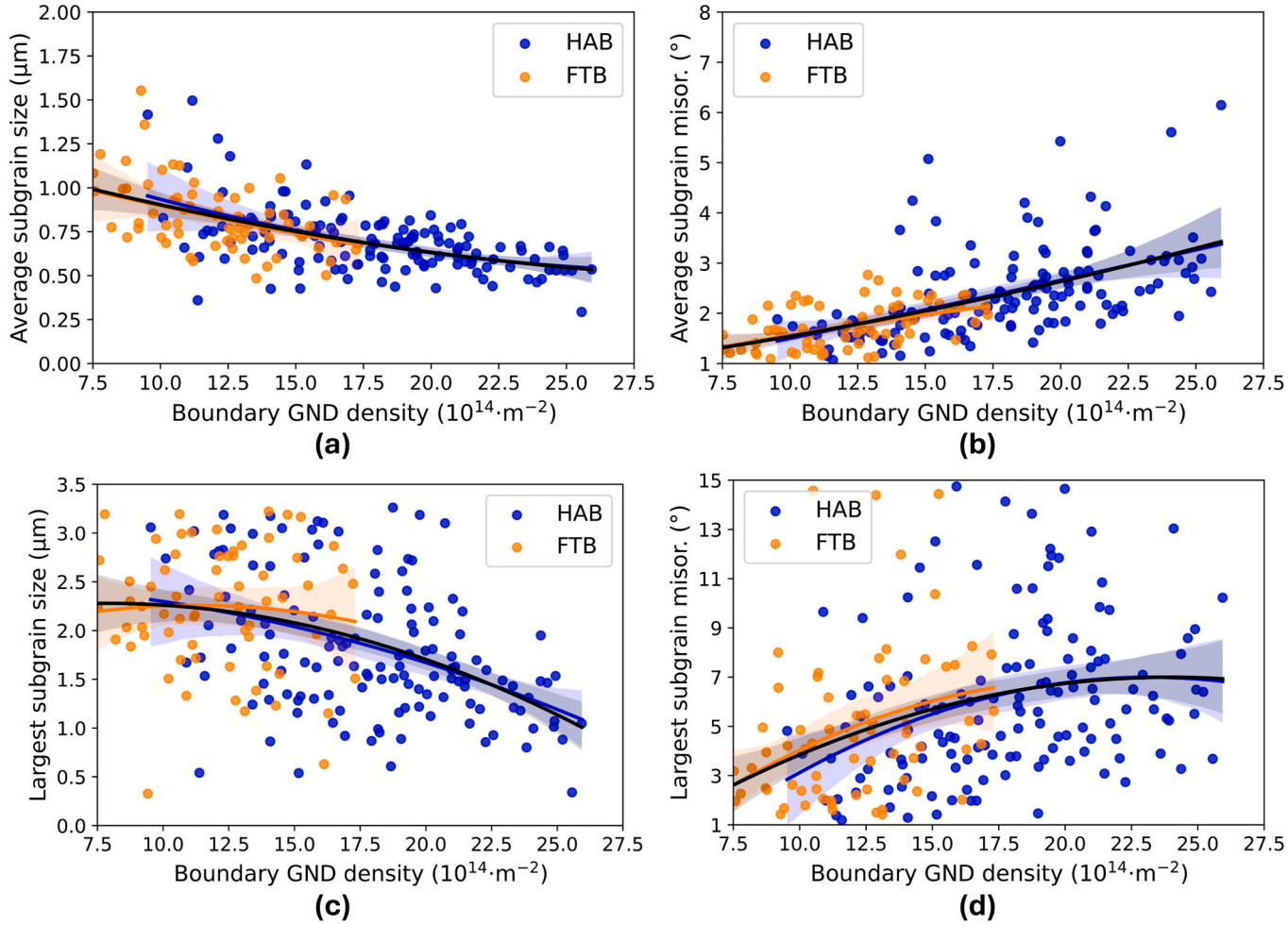

Fig. 7. Characteristics of the substructure surrounding individual deformed grain boundaries as a function of the corresponding boundary GND density: (a) average subgrain size, (b) average subgrain misorientation, (c) size of the largest subgrain, and (d) largest subgrain misorientation. The solid lines account for polynomial regression fits (order equal to two), and have been added for visual guidance only. The shaded surrounding areas represent a confidence interval for the fits, with a confidence index of 95%. Blue markers and lines correspond to general high-angle boundaries (HAB), and orange ones to former twin boundaries (FTB). The black line displays the combined effect of general HABs and FTBs. (For interpretation of the references to colour in this figure legend, the reader is referred to the web version of this article.)

slopes obtained for both the average and the largest subgrain misorientations confirm that the correlations are significant: $(+0.11 \pm 0.02)\cdot10^{-14}$ °/m^{-2} and $(+0.24 \pm 0.09)\cdot10^{-14}$ °/m^{-2}, respectively.

To further investigate the relationship between boundary dislocation density and the resultant substructure, the deformed grain boundaries in the examined EBSD maps have been divided into groups, depending on their GND density level. Particularly, four categories have been created, having increasingly higher boundary GND densities (ρ_{GB}-1 < ρ_{GB}-2 < ρ_{GB}-3 < ρ_{GB}-4), and roughly the same number of boundaries each. The boundary GND density range corresponding to each category, as well as the resultant number of boundaries, is shown in Table 3. Table 3 indicates also the average subgrain-free boundary length fraction within the four categories. In line with the discussion in Section 3.1, these fractions decrease with higher boundary GND density of the category, and the decrease tends to saturate for the categories with higher GND densities. In turn, this reduction in the subgrain-free length fractions implies a larger number of captured subgrains within the category, with higher boundary GND density (Table 3). The magnitude of the increase is also reduced gradually with higher boundary GND density. Moreover, the number of captured subgrains even decreases from the third to the fourth category, despite the subgrain-free length fraction still decreasing. The reason for this behavior is the decrease of the total boundary length inside each category (also given in Table 3) with higher boundary GND density: as shown in Section 3.1, higher boundary GND densities are possible for boundaries with shorter captured lengths (Fig. 4(a)). In addition, Table 3 provides the average subgrain size and misorientation within each boundary GND density category. In accordance with Fig. 7(b), the average subgrain misorientation monotonically increases with higher GND density of the category. At the same time, the subgrain size decreases, in agreement with Fig. 7(a). The size and misorientation distributions including all the subgrains inside each category are shown in Fig. 8, and exhibit similar trends. The figure indicates that the fraction of subgrains with smaller misorientations than 2° decreased steadily with higher GND density of the category; at the same time, the fraction of subgrains with larger misorientations increased (Fig. 8(b)). Similarly, the fraction of subgrains with smaller sizes than 0.75 μm became gradually higher with increasing GND density (Fig. 8(a)). This effect was more pronounced for subgrains with smaller sizes than 0.5 μm.

Table 3
Mean diameter and misorientation of subgrains located at grain-boundary sites, for boundaries within four different boundary GND density ρ_{GB} categories: ρ_{GB}-1 ($\rho_{GB} \leq 1.25\cdot10^{15}$ m^{-2}), ρ_{GB}-2 ($1.25\cdot10^{15}$ m^{-2} < $\rho_{GB} \leq 1.60\cdot10^{15}$ m^{-2}), ρ_{GB}-3 ($1.60\cdot10^{15}$ < $\rho_{GB} \leq 1.95\cdot10^{15}$ m^{-2}) and ρ_{GB}-4 ($\rho_{GB} > 1.95\cdot10^{15}$ m^{-2}). The number of boundaries and grain-boundary subgrains in each category is also given, together with the aggregate values corresponding to all the boundaries. The uncertainties indicated are the standard errors considering the number of boundaries and subgrains analyzed, respectively.

Category of boundary GND density	ρ_{GB}-1	ρ_{GB}-2	ρ_{GB}-3	ρ_{GB}-4	Total
Lower limit (m^{-2})	0	$1.25\cdot10^{15}$	$1.60\cdot10^{15}$	$1.95\cdot10^{15}$	–
Upper limit (m^{-2})	$1.25\cdot10^{15}$	$1.60\cdot10^{15}$	$1.95\cdot10^{15}$	∞	–
No. of boundaries analyzed	52	52	52	51	207
Boundary length analyzed (mm)	2.88	2.29	1.64	1.10	7.91
Mean subgrain-free boundary length fraction	0.48 ± 0.03	0.23 ± 0.02	0.12 ± 0.02	0.06 ± 0.01	0.25 ± 0.02
No. of subgrains analyzed	938	1192	1223	1088	4441
Mean subgrain diameter (μm)	0.87 ± 0.02	0.75 ± 0.02	0.68 ± 0.01	0.61 ± 0.01	0.72 ± 0.01
Mean subgrain misorientation (°)	1.61 ± 0.04	2.03 ± 0.05	2.27 ± 0.05	2.69 ± 0.06	2.17 ± 0.02

The observed trend between boundary GND density and subgrain misorientation agrees with the general trend found in the literature between subgrain misorientation and applied strain (for the subgrains located in deformed grain interiors) [2,6,7,34–36,38]. As higher applied strains lead to higher dislocation densities [3], an equivalent effect on substructure development is expected for both. This trend between boundary GND density and subgrain misorientation is also in line with the expectation, following the description of LABs as dislocation arrays: LABs with higher misorientations contain dislocations that are more closely spaced within the boundary [3]; for equal subgrain boundary area, a higher density of dislocations thus implies subgrain boundaries with higher misorientations.

On the other hand, previous substructure characterization studies have found conflicting trends between applied strain and subgrain size (for the subgrains in the deformed grain interiors). Below a certain strain, subgrain sizes decrease with higher dislocation density [2,7,34–37,55]. This is a natural effect, if LABs are considered as dislocation arrays: smaller subgrains mean a higher density of subgrain boundaries per unit of volume; for equal subgrain boundary misorientations, smaller subgrains can thus accommodate a higher dislocation density. However, above a certain strain, subgrain sizes cease to decrease, and stay essentially unchanged against any further dislocation density increase. When that occurs, higher dislocation density translates into a higher subgrain misorientation only [1,5–7,62]. At the same time, as displayed for this case, dislocation densities around deformed grain boundaries can be considerably higher than in the grain interiors. In fact, higher average subgrain misorientation and smaller subgrain size have been found here around deformed grain boundaries than Taylor *et al.* did in the deformed grain interiors, for the higher strain of 1 [34] (~2.2° and ~0.7 μm here, see Table 3, against ~1.7° and ~1.2 μm in [34]). The data by Taylor *et al.* were also obtained for Ni-30%Fe, and under similar deformation conditions to the present ones (900 °C and 1 s^{-1} [34]). Consequently, the comparison with Taylor *et al.* [34] suggests that the dislocation density is higher around deformed grain boundaries for a strain of 0.2 than in the deformed grain interiors for a strain of 1. These relatively high dislocation densities around deformed grain boundaries could thus conceivably exceed the level required for the subgrain size to saturate. Yet, the present results demonstrate that this is not the case: the size of the subgrains surrounding the deformed grain boundaries decreases steadily as the dislocation density around the boundary increases.

Nevertheless, this reduction in the average subgrain size per boundary with boundary dislocation density is at odds with results presented in [29]. Those were obtained for the same microstructure examined here, but excluding the subgrain boundaries with lower misorientations than 1° from the analysis. With that condition in place, the average subgrain size per boundary is essentially independent of boundary dislocation density [29]. Hence, the present results also imply that the decrease in subgrain size with higher dislocation density is solely produced by the subgrain boundaries with lower misorientations than 1°. In other words, that decrease is exclusively caused by incidental dislocation boundaries (IDBs). IDBs result from the statistical mutual trapping of gliding dislocations, and are opposed to geometrically necessary boundaries (GNBs). The latter form due to different slip system activities, or levels of shear strain, on both sides of the GNB [74,91]. Former studies on cold-deformed metals have found that the vast majority of IDBs possess lower misorientations than 1° [91]. At the same time, GNB misorientations are nearly always larger than 1°, regardless of the level of applied strain [91].

3.3.2. The effect of the type of nucleation site

This subsection compares the properties of the subgrains located at different types of nucleation sites around deformed grain boundaries (i.e., subgrains with at least two neighboring deformed grains). Particularly, Table 2 indicates that a significant fraction of those subgrains (141

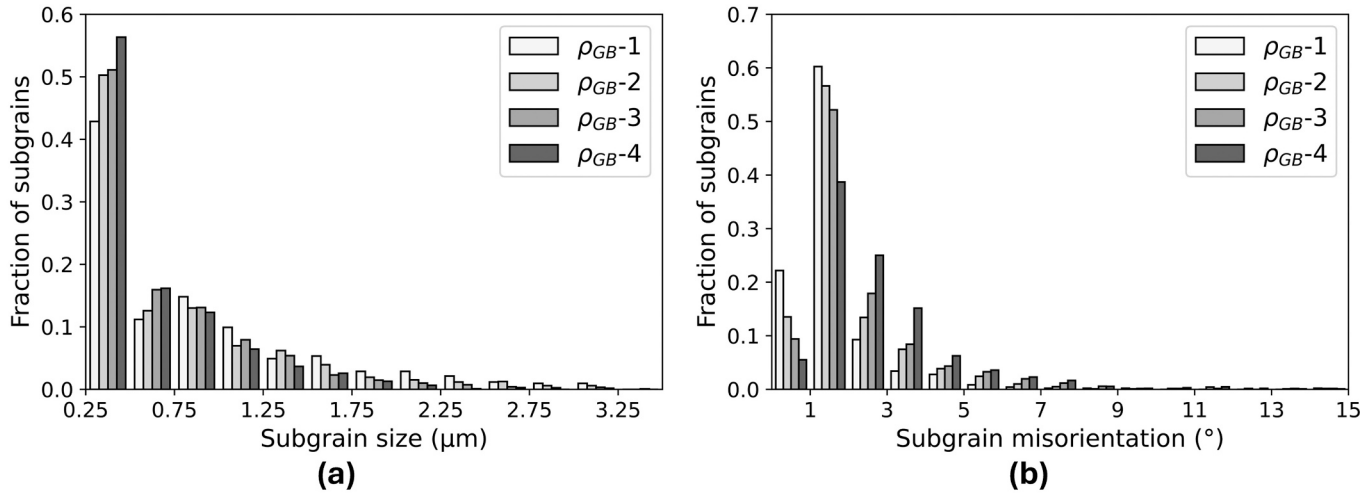

Fig. 8. Distribution of (a) the sizes and (b) the misorientations of the subgrains lying around deformed grain boundaries, classified into four categories depending on the GND density of the boundary ρ_{GB} to which they belong: ρ_{GB}-1 ($\rho_{GB} \leq 1.25{\cdot}10^{15}$ m^{-2}), ρ_{GB}-2 ($1.25{\cdot}10^{15}$ m$^{-2} < \rho_{GB} \leq 1.6{\cdot}10^{15}$ m^{-2}), ρ_{GB}-3 ($1.6{\cdot}10^{15} < \rho_{GB} \leq 1.95{\cdot}10^{15}$ m^{-2}) and ρ_{GB}-4 ($\rho_{GB} > 1.95{\cdot}10^{15}$ m^{-2}).

out of 4591, i.e., ~3%) was adjacent to a triple junction of deformed grains (subgrains with exactly three neighboring deformed grains). By contrast, less than 0.1% (9 out of 4591) neighbored a quadruple junction of deformed grains (subgrains with exactly four neighboring deformed grains). The rest of those subgrains (4441 out of 4591) belonged to grain-boundary sites (subgrains with exactly two neighboring deformed grains). In view of the small number of quadruple-junction subgrains captured, this subsection focuses on the subgrains located at grain-boundary and triple-junction nucleation sites.

The subgrain size and misorientation distributions separately encompassing subgrains located at those two nucleation site types can be viewed in Fig. 6(c)-(d). The two size distributions are very similar to each other (Fig. 6(c)). Accordingly, the average subgrain sizes of triple-junction and grain-boundary subgrains do not differ significantly (~0.7 μm for both, see Table 2). Yet, the fraction of subgrains with the largest sizes (i.e., larger than 1.75 μm) is distinctly higher for triple-junction sites. This is compensated for by the fraction of the smallest grains (i.e., smaller than 0.5 μm) being also higher for triple-junction subgrains. The latter effect even resulted in a smaller average subgrain size for the detected quadruple-junction subgrains (Table 2). On the other hand, the misorientation distribution of triple-junction subgrains deviates significantly from that of the grain-boundary subgrains (Fig. 6(d)). Specifically, the former is shifted to considerably larger values: the misorientations of most grain-boundary subgrains are smaller than 3°, whereas those of triple-junction subgrains are more balanced across the LAB range (Fig. 6(d)). Consequently, the average misorientation of the triple-junction subgrains is significantly larger than that of the grain-boundary subgrains (~3.6° against ~2.2°, Table 2). Quadruple-junction subgrains exhibited an even larger average misorientation (Table 2).

These results can explain the preferential role previously attributed to triple-junction sites in the nucleation of SRX in hot-deformed austenite [52,63,64]. In fact, for a given deformed grain boundary, SRX nucleation preferentially initiates at the triple junctions rather than at any grain-boundary site [43]. In this respect, SRX nucleation takes place when the LAB between a subgrain and its parent deformed grain fully transforms into an HAB, after the progressive increase of the LAB misorientation [29]. The transformation into an HAB confers relatively high mobility to the boundary, making it possible for the nucleus to grow into the adjacent deformed grains [29]. With this mechanism, subgrains with initially higher boundary misorientations possess a nucleation advantage: they can more easily reach the minimum HAB misorientation (typically, 15° [3]) in the incubation time before SRX. In this case, the fraction of subgrains with misorientations relatively close to the HAB threshold is significantly higher at triple-junction sites than at grain-boundary sites (note the higher fractions of larger misorientations than, e.g., 5 or 10° in Fig. 6(d)). Therefore, triple-junction sites are more likely to readily produce nucleation, as observed in practice. The present results also highlight the degree of success of triple-junction sites in terms of SRX nucleation: when subjecting the present microstructure to SRX, about half of the new grains appear at triple junctions, and the other half at grain-boundary sites [43]; yet, the number of subgrains existing at triple junctions is more than thirty times smaller than the number of subgrains at grain-boundary sites (Table 2). Hence, a triple-junction subgrain is over thirty times more likely to produce a nucleation event than a grain-boundary one. Of course, this comparison is affected by the existence of subgrain-free regions around deformed grain boundaries. However, these occur more often near grain-boundary sites than near triple junctions (e.g., Fig. 2(b)). As a result, the relative nucleation efficiency of triple junctions would be even higher, if understood in terms of the boundary length (or area) available as subgrains. Additionally, if the relationship between subgrain misorientations and boundary dislocation density shown in Section 3.3.1 is recalled, the reason for the larger misorientations at triple junctions is clear: higher dislocation densities accumulated around them, compared to grain-boundary sites (Section 3.1 and Fig. 3(a)-(b)).

By contrast, the comparison between the size distributions of triple-junction and grain-boundary subgrains is more complex (Fig. 6(c)): triple junctions showed higher fractions of both the smallest and largest subgrains, compared to grain-boundary sites. On the one hand, the higher fraction of relatively small subgrains agrees with the general effect of dislocation density on subgrain size as discussed in Section 3.3.1. In virtue of that effect, the higher dislocation density around triple junctions (Section 3.1) leads to increased fragmentation into subgrains of the SIBM bulges located at those sites. For instance, Fig. 9(a)-(b) shows a bulge located at a triple grain junction and fragmented into three smaller subgrains.

Nevertheless, not all the observed triple-junction bulges exhibited fragmentation into subgrains. Some were composed of one subgrain only (e.g., Fig. 9(c)-(d)), with the LAB of that subgrain located at the base of the bulge (yellow arrow in Fig. 9(d)). These triple-junction bulges explain the higher fraction of the largest subgrains found at triple junctions. The reason is the enhanced tendency for SIBM at multiple grain junctions, relative to grain-boundary sites [29]. That tendency can lead to relatively large bulge amplitudes during deformation already, which increase the size of the corresponding (non-fragmented) multiple-

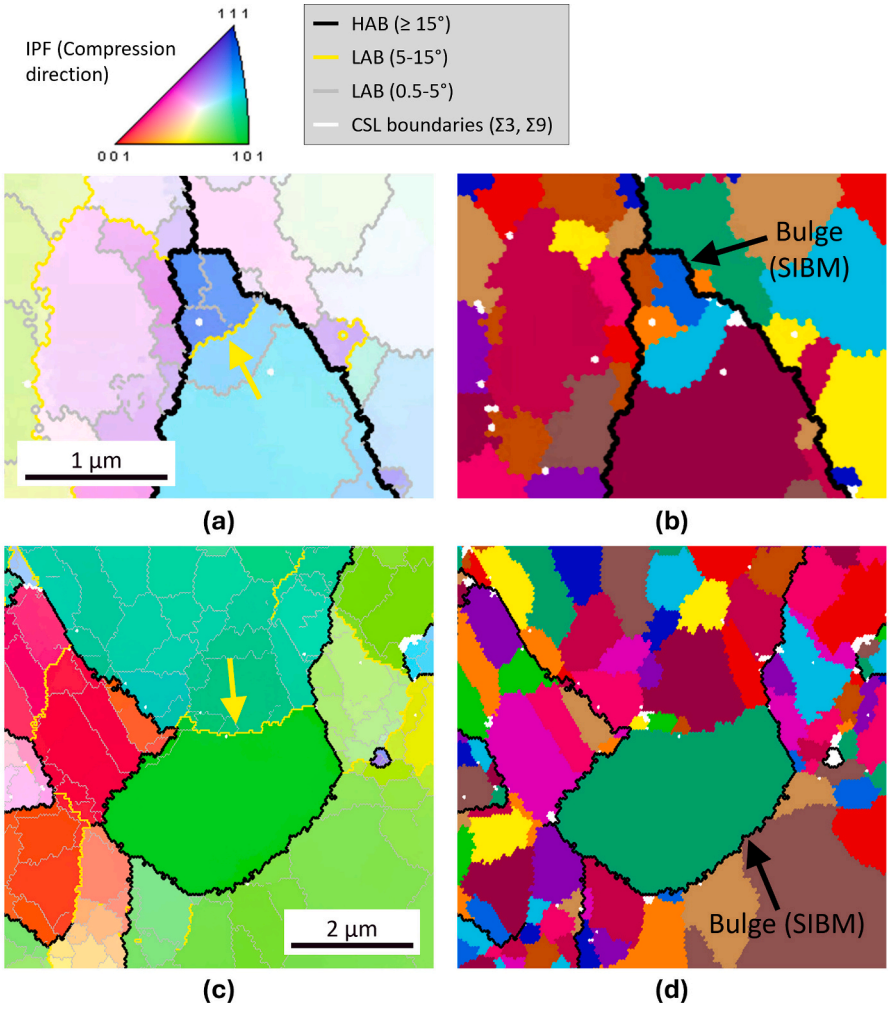

Fig. 9. Example of SIBM bulges located at triple grain junctions, which (a, b) exhibit and (c, d) do not exhibit fragmentation into smaller subgrains: (a, c) IPF map, and (b, d) subgrain map, where each colour represents one of the entities resulting from the deformed grains' discretization into subgrains and parent grains. White lines indicate Σ3 and Σ9 CSL boundaries (i.e., twin boundaries). Black lines indicate boundaries with misorientations higher than 15°, and not identified as CSL boundaries (i.e., general HABs). Yellow lines indicate boundaries with misorientations between 5 and 15° (i.e., LABs). Gray lines indicate boundaries with misorientations between 0.5 and 15° (i.e., LABs). The gray and yellow lines have been omitted from (b) and (d). The yellow arrows in (a) and (c) point at the LAB located at the base of the bulge. (For interpretation of the references to colour in this figure legend, the reader is referred to the web version of this article.)

junction subgrains. At the same time, LABs stay immobile before SRX nucleation [29]. Hence, they do not contribute to a larger size of multiple-junction subgrains. A clear example of the enhanced SIBM (bulging) at multiple grain junctions can be viewed in Fig. 10. The EBSD map of this figure was obtained with a coarser step size than the others in this study: 0.5 μm. Fig. 10 displays two adjacent bulges of the same parent deformed grain, both growing into the same neighboring deformed grain: one is located at a quadruple grain junction, and the other one at a grain-boundary site. The figure shows a much larger amplitude for the quadruple-junction bulge than for the grain-boundary one (~9 μm against ~4 μm). Furthermore, the position of the LAB enclosing the quadruple-junction bulge (gray arrow, average misorientation across the LAB of ~4°) roughly corresponds to the base of the bulge. This confirms the absence of migration of that LAB. The LABs at the base of the triple-junction bulges in Fig. 9 suggest the same lack of migration (yellow arrows in the figure). In turn, the enhanced bulging at multiple grain junctions is due to two reasons [43]: (i) the higher dislocation densities around them (Section 3.1), which accelerate the rate of bulging [23,24]; and (ii) the consumption of 'extra' deformed grain boundaries as the bulges migrate, which are not present at grain-boundary sites [43]. The latter provides an energetic advantage through the removal of the corresponding boundary energy, and of the higher dislocation densities surrounding deformed grain boundaries [43]. For the quadruple-junction bulge in Fig. 10, the 'extra' deformed grain boundaries are a general HAB and an FTB (the boundary in the left upper corner which is partly a white line and partly a black line).

3.3.3. *The effect of the type of deformed grain boundary*

The differences between the sizes and misorientations of the subgrains located around general HABs and FTBs are examined in this subsection. In this regard, the plots in Fig. 7 contain the average and maximum values of each property for all the deformed grain boundaries belonging to each type. In the four plots, the results considering general HABs only (blue lines in Fig. 7(a)-(d)) essentially overlap those considering FTBs only (orange lines in Fig. 7(a)-(d)). A similar conclusion can be drawn from Fig. 5(a), in terms of the subgrain-free length fractions for both boundary types. These observations imply that, despite their distinctly different dislocation transmission properties (Section 3.1), substructure development (and the associated recovery processes) does not significantly differ around FTBs and general HABs (for the dislocations that do accumulate around the boundary). This is relevant for, e.g., the input to microstructural models incorporating topology (e.g., cellular automata). For example, topology-based models of recrystallization aim to predict the nucleation rate from the aggregate behavior of

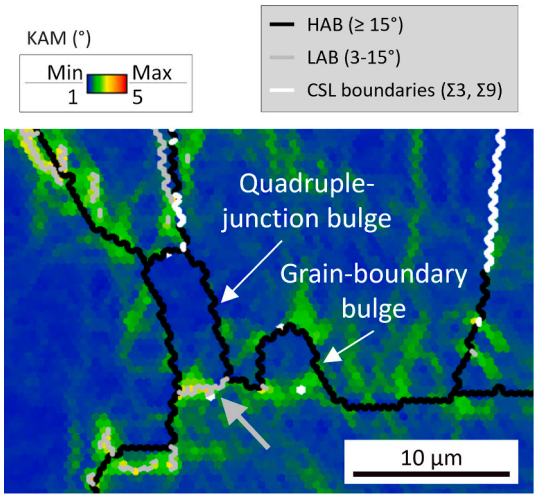

Fig. 10. KAM map displaying an example of SIBM bulges formed at adjacent quadruple-junction and grain-boundary nucleation sites. White lines indicate Σ3 and Σ9 CSL boundaries (i.e., twin boundaries). Black lines indicate boundaries with misorientations higher than 15°, and not identified as CSL boundaries (i.e., general HABs or FTBs). Gray lines indicate boundaries with misorientations between 3 and 15° (i.e., LABs). The gray arrow indicates the LAB at the base of one of the bulges.

all the subgrains within a deformed microstructure [25–27]. Because of the increase of the subgrain misorientations with higher GND density (Section 3.3.1) and the lower boundary GND densities of FTBs (Section 3.1 and Fig. 3(a) and (c)), the average subgrain misorientation for FTBs is significantly lower than for general HABs (~1.9° against ~2.3°, Table 1). On the other hand, the reduction in subgrain size with increasing boundary GND density (Section 3.3.1) means that the average subgrain size displayed by FTBs is significantly larger than that of general HABs (~0.8 µm against ~0.7 µm, Table 1).

These results can explain the considerably lower nucleation efficiencies (i.e., number of SRX grains formed per boundary length unit) formerly reported for FTBs in the SRX of austenite, compared to general HABs [43]. These lower nucleation efficiencies lead to FTBs making a minor contribution to SRX nucleation in austenite only [43,52]. Firstly, the number of subgrains per boundary length unit is much smaller around FTBs: only around two thirds of those existing for general HABs (Table 1). This is despite the total boundary length in the microstructure being somewhat larger for FTBs (Table 1). Because SRX grains form from subgrains, the existence of fewer subgrains directly means fewer opportunities for nucleation. Secondly, the misorientations of the subgrains tend to be smaller around FTBs (Table 1 and Fig. 7(b) and (d)). As pointed out in Section 3.3.2, larger subgrain misorientations are closer to the HAB misorientation threshold (typically, 15° [3]). Hence, those subgrain boundaries can more readily transform into HABs in the initial stages of recrystallization. This gives rise to effective nucleation, because of the higher boundary mobility associated [29]. Additionally, both reasons for the lower nucleation efficiency (fewer subgrains and lower subgrain misorientations) can be attributed to the lower GND densities accumulated around FTBs (see Fig. 5(a) and Fig. 7(b) and (d), respectively). This is owing to the special dislocation transmission properties of twin boundaries, as explained in Section 3.1. Nevertheless, although comparatively less than general HABs, FTBs also produce nucleation [43]. This is consistent with the present results: subgrain misorientations near the HAB threshold (e.g., larger than 5 or 10°) exist for FTBs in Fig. 7(d), albeit less frequently than for general HABs.

3.4. Quantitative description of the substructure

In this section, the application of physics-based equations to relate the average subgrain sizes and misorientations around a deformed grain boundary with the corresponding boundary dislocation density is examined. Such equations are required by the development of microstructural models, able to incorporate the far-reaching implications of the substructure on the behavior of metals.

3.4.1. Average subgrain sizes

In the literature, the relationship between subgrain size and dislocation density has most often been modelled via a Staker-Holt equation (e.g., [11,27,56–61]). Staker-Holt relationships assume an inverse proportionality between the average subgrain size and the square root of the average dislocation density [37]. For the subgrains located around one deformed grain boundary, a Staker-Holt equation can be defined as:

$$\overline{d}_{SG} = \frac{K_{SH-GB}}{\sqrt{\rho_{GB}}} \tag{1}$$

where $\overline{d}_{SG}$ and ρ_{GB} are the average subgrain size and dislocation density around the boundary, and K_{SH-GB} is the Staker-Holt constant for subgrains located around deformed grain boundaries. The K_{SH-GB} values obtained for the deformed grain boundaries analyzed in this study are plotted in Fig. 11(a). The figure indicates that the K_{SH-GB} value obtained for a single boundary is, on average, independent of the boundary GND density (slope of the linear fit equal to $(-0.06 \pm 0.18)\cdot10^{-14}$ $1/m^{-2}$). In other words, roughly the same Staker-Holt constant value applies within the whole examined boundary dislocation density range. This means that, like the subgrains in the deformed grain interiors, those surrounding the deformed grain boundaries also follow a Staker-Holt relationship. Fig. 11(a) also displays significant scatter within a given level of boundary dislocation density. Nevertheless, this scatter is intrinsic to the examined effect: the length of the grain boundaries in a material with an engineering grain size is limited. Consequently, the number of subgrains that can be located around each of those boundaries is also limited. In addition, Fig. 11(a) suggests that the same average K_{SH-GB} value applies to the subgrains surrounding general HABs and FTBs. This is in line with the other results shown in this study, which suggested an equivalent quantitative behavior for both boundary types for the same boundary dislocation density level.

Fig. 11(b) displays the distribution of the Staker-Holt constant values found for the individual deformed grain boundaries. The vast majority of the K_{SH-GB} values were comprised between 20 and 40. The average value across all the studied boundaries was equal to 28.6 ± 0.4. This is close in magnitude to the value of 35 estimated by Shah *et al.* in [27], also for hot-deformed austenite and subgrain sizes and dislocation densities surrounding deformed grain boundaries. The K_{SH-GB} of 35 was the average value in the microstructure leading to accurate predictions of the grain size after DRX and MDRX, with the physics-based model proposed by the authors [27]. Hence, it was not experimentally measured, like in the present study. Besides, the deformation temperatures and applied strain were higher than those employed here (950–1100 °C and 0.5 [27]). On the other hand, both K_{SH-GB} values are considerably higher than the original value of the Staker-Holt constant reported by Staker and Holt (i.e., 16 [37]). Their study considered pure copper, and only subgrains in deformed grain interiors [37]. Unlike those, subgrains surrounding deformed grain boundaries form under a dislocation density gradient, with respect to the distance to the boundary (see Fig. 3(a)). Moreover, Staker and Holt obtained their value for a deformation temperature range between 25 and 700 °C [37]. By contrast, later studies have shown that the Staker-Holt constant value increases with higher deformation temperature [56]. Specifically, a value of 24 has been reported for pure copper after deformation at a temperature as low as 400 °C (for the subgrains in the deformed grain interiors) [56].

All in all, the present results demonstrate that a Staker-Holt relationship can be applied not only to describe the average subgrain sizes in deformed grain interiors, but also those adjacent to deformed grain

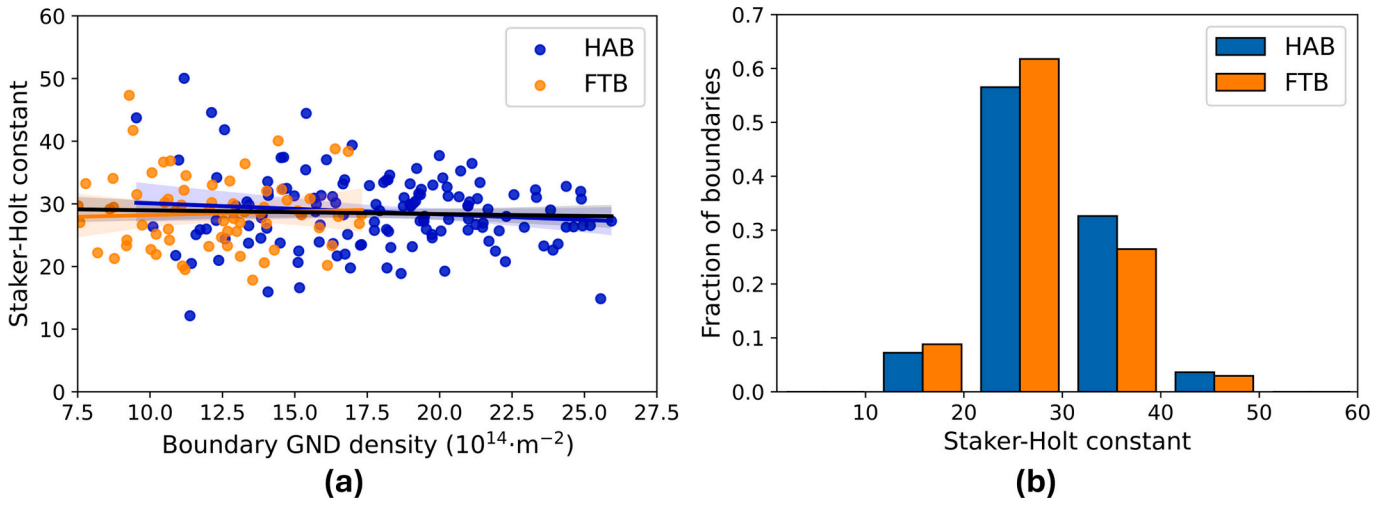

Fig. 11. (a) Staker-Holt constant value for each of the analyzed deformed grain boundaries as a function of the corresponding boundary GND density. (b) Distribution of the Staker-Holt constant values for each of the analyzed deformed boundaries. The solid lines in (a) account for linear regression fits, and have been added for visual guidance only. The shaded surrounding areas represent a confidence interval for the fits, with a confidence index of 95%. Blue markers and lines correspond to general high-angle boundaries (HAB), and orange ones to former twin boundaries (FTB). The black line displays the combined effect of general HABs and FTBs. (For interpretation of the references to colour in this figure legend, the reader is referred to the web version of this article.)

boundaries. This is despite the fact that subgrains neighboring deformed grain boundaries form under dislocation density gradients with respect to the distance to the grain boundary. Such gradients do not exist in deformed grain interiors (Fig. 3(a)-(b)). Moreover, the Staker-Holt relationship is applicable around deformed grain boundaries also despite the higher dislocation densities in that region (Section 3.1). Those could have reached the level at which subgrain sizes cease to decrease with higher dislocation density [1,5–7,62]. Yet, the present study shows that this is not the case. Additionally, the current results suggest that, in the present case, the Staker-Holt behavior (and the decreasing trend of subgrain size with higher dislocation density in general, Section 3.3.1) is caused by the IDBs solely (i.e., subgrain boundaries with lower misorientations than 1°, Section 3.3.1), and not by the GNBs. This can be rationalized by the association between Staker-Holt behavior and the dislocation-dislocation interaction distance made in [37]: only IDBs are created by the incidental interaction between the dislocations periodically generated during plastic deformation. By contrast, GNBs separate areas in the microstructure subjected to different strain constraints [74,91]. As the present study implies, a higher overall dislocation density around the boundary does not necessarily mean a larger density of those areas (and, thus, a smaller spacing between consecutive GNBs).

3.4.2. *Average subgrain misorientations*

Regarding the relationship between average subgrain misorientation and boundary dislocation density, the data in Fig. 7(b) indicate that a direct correlation exists between both variables. In this view, a physics-based expression approximating that relationship is derived in this section. To this end, it is assumed that all the GNDs located around a deformed grain boundary are distributed into subgrain boundaries after deformation. In other words, the contribution to the GND density of GNDs located in subgrain interiors is ignored. This is reasonable, considering the TEM analysis in [52]: that study found subgrain interiors to be essentially dislocation-free.

To obtain the intended expression, an identification is thus made between the total number of dislocations $N_{dis-LAB}$ forming the boundaries of all the subgrains adjacent to a deformed grain boundary, and the overall number of dislocations N_{dis-GB} in the material layer surrounding the deformed grain boundary (as derived from the average dislocation density ρ_{GB} measured around the boundary). This situation is sketched in Fig. 12(a). Although the subgrains are represented as semicircles in the figure, no assumption is made about their shape, other than being entities with the equivalent circle diameter d_{SG} measured by EBSD (Section 2.2).

The number of dislocations N_{dis} making up an individual subgrain boundary with length L_{SG} and misorientation θ_{SG} can be derived as [4]:

$$N_{dis} = \frac{L_{SG}}{b}\theta_{SG} \tag{2}$$

where b is the length of the Burgers vector of the dislocations. In Eq. (2), θ_{SG} is expressed in radians (i.e., θ_{SG} must be multiplied by $\pi/180$ before entering the equation, if given in degrees).

Therefore, the average number of dislocations $\overline{N}_{dis}$ making up the individual subgrain boundaries surrounding a deformed grain boundary can be obtained replacing $L_{SG}\theta_{SG}$ by the average product of the lengths and misorientations of those subgrain boundaries $\overline{L_{SG}\theta_{SG}}$:

$$\overline{N}_{dis} = \frac{\overline{L_{SG}\theta_{SG}}}{b} \tag{3}$$

$\overline{L_{SG}\theta_{SG}}$ can then be approximated by the product of the individual averages $\overline{L}_{SG}\overline{\theta}_{SG}$. $\overline{L}_{SG}$ is the average length of the subgrain boundaries surrounding the deformed grain boundary, and $\overline{\theta}_{SG}$ is their average misorientation. At the same time, $\overline{L}_{SG}$ can be replaced by $\pi\cdot\overline{d}_{SG}$. The replacement of the average product by the product of the averages is justified in detail in Appendix A. In any case, average values of 27.21 nm and 27.27 nm were measured here for $\overline{d_{SG}\theta_{SG}}$ and $\overline{d}_{SG}\overline{\theta}_{SG}$ across the examined deformed grain boundaries. This means an average error of ~0.2% only due to the replacement.

Considering this, the total number of dislocations $N_{dis-LAB}$ making up the boundaries of all the subgrains located around the deformed grain boundary can be calculated as:

$$N_{dis-LAB} = \frac{\pi\overline{d}_{SG}}{b}\overline{\theta}_{SG}\cdot N_{SG} \tag{4}$$

where N_{SG} accounts for the number of subgrains surrounding the deformed grain boundary.

If the deformed grain is considered to be of circular shape, and to have a diameter equal to the average (deformed) grain size $\overline{D}_G$, N_{SG} can be derived from $\overline{d}_{SG}$ as:

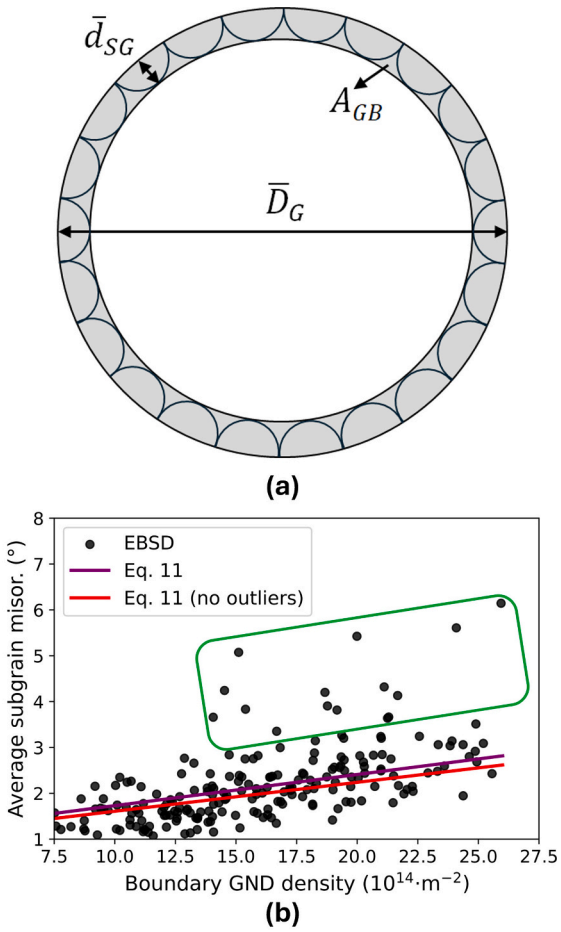

Fig. 12. (a) Geometry assumed for the derivation of Eq. (11), in which subgrains with an equivalent circle diameter $\overline{d}_{SG}$ surround the boundary of a deformed grain having a diameter $\overline{D}_G$. The gray area represents the area A_{GB} of the layer within which the boundary GND density ρ_{GB} has been measured. (b) Comparison between the average subgrain misorientations measured around individual deformed grain boundaries by EBSD and the corresponding description by Eq. (11) (Eq. (11), purple line). The green box encircles relative outlier points. The result from Eq. (11) is also given, when those outlier points are excluded from the fitting of the equation (red line). (For interpretation of the references to colour in this figure legend, the reader is referred to the web version of this article.)

$$N_{SG} = \frac{\pi \overline{D}_G}{\overline{d}_{SG}} \tag{5}$$

Combining Eqs. 4 and 5, $N_{dis-LAB}$ is then obtained as:

$$N_{dis-LAB} = \frac{\pi^2 \overline{D}_G}{b} \overline{\theta}_{SG} \tag{6}$$

On the other hand, the total number of dislocations N_{dis-GB} surrounding the deformed grain boundary can be derived as the product of its boundary dislocation density ρ_{GB}, and the area A_{GB} of the layer around the boundary within which the dislocations are considered (gray in Fig. 12(a)). If the thickness of that layer is equal to $\overline{d}_{SG}$, N_{dis-GB} is given by:

$$N_{dis-GB} = \rho_{GB} A_{GB} = \rho_{GB} \frac{\pi}{4} \left(\overline{D}_G^2 - (\overline{D}_G - \overline{d}_{SG})^2 \right) \tag{7}$$

which can be simplified, considering that $\overline{d}_{SG} << \overline{D}_G$:

$$N_{dis-GB} = \frac{\pi}{2} \rho_{GB} \overline{D}_G \overline{d}_{SG} \tag{8}$$

Taking thus $N_{dis-LAB}$ equal to N_{dis-GB}, Eqs. 6 and 8 lead to:

$$\overline{\theta}_{SG} = \frac{b \overline{d}_{SG}}{2\pi} \rho_{GB} \tag{9}$$

Nevertheless, Eq. (9) assumes that the entire subgrain boundaries can contain dislocations. This is not true: since the equation refers to the subgrains surrounding a deformed grain boundary, a part of those subgrain boundaries possesses HAB character (i.e., the part separating the subgrain from the neighboring deformed grain). This fraction of the subgrain boundary lengths cannot contain dislocations. Additionally, the subgrain boundary misorientations in this study have been derived taking into account, for each subgrain, the whole fraction of its boundary length that is an LAB. However, a part of that length fraction may be shared with other subgrains also neighboring the deformed grain boundary. In the dislocation balance of Eq. (4), that part would be counted twice, one for each neighboring subgrain. The rest of the subgrain boundary fraction that is an LAB is shared with the parent grain, or with subgrains not neighboring the deformed grain boundary.

Consequently, to apply the expression to the current data, $\overline{d}_{SG}$ is replaced in Eq. (9) by an effective subgrain size. This is smaller than $\overline{d}_{SG}$ by a geometric factor called z (with $z > 1$). z accounts for the fraction of the subgrain boundaries that has HAB character, or may be shared with other subgrains that are also located around the deformed grain boundary:

$$\overline{\theta}_{SG} = \frac{b \overline{d}_{SG}}{2\pi z} \rho_{GB} \tag{10}$$

Finally, Eq. (10) can be further simplified considering the Staker-Holt relationship between $\overline{d}_{SG}$ and ρ_{GB} (Eq. (1)). This was shown to hold in Section 3.4.1:

$$\overline{\theta}_{SG} = \frac{b K_{SH-GB}}{2\pi z} \sqrt{\rho_{GB}} \tag{11}$$

About z, its average value for the deformed grain boundaries in the analyzed microstructure can be estimated from the experimental measurements. To this end, $\overline{\theta}_{SG}$ and ρ_{GB} are substituted in Eq. (11) by the average subgrain misorientation and boundary GND density here measured across all the boundaries. The values including both general HABs and FTBs are considered (2.17° and $1.60 \cdot 10^{15}$ m^{-2}, see Table 1). For a Burgers vector length of 0.2518 nm [86], and the measured average Staker-Holt constant K_{SH-GB} of 28.6 (Section 3.4.1), this leads to a value of z equal to 1.21. Such a value suggests that only a limited fraction of the total subgrain boundary length is shared with other subgrains also neighboring the deformed grain boundary. This agrees with the observed subgrains in the present EBSD maps (e.g., Fig. 1). Moreover, this is also consistent with the circular shape assumed for the subgrains in the derivation of Eq. (11) (Fig. 12(a)).

The validity of Eq. (11) is tested against the average subgrain misorientations measured for the deformed grain boundaries examined in the present case (the same data plotted in Fig. 7(b)) via Fig. 12(b). The equation provides a good approximation (purple line in Fig. 12(b)) to the average boundary behavior, except for the boundaries located outside the main point cloud (i.e., those encircled by the green box). These "outliers" correspond to boundaries for which a very small number of subgrains was detected (typically, less than ten), and for which those subgrains were characterized by relatively large misorientations. Nevertheless, Fig. 12(b) also includes the result of Eq. (11) when the "outliers" are excluded from the fitting (red line in the figure). In that case, the value of z is 1.31. The figure indicates that the difference made by the outliers in Eq. (11) is only minor. In addition, scatter also exists, albeit smaller, among the boundaries located inside the main point cloud. That scatter is also due to each boundary being surrounded by a limited number of subgrains. This is intrinsic to the examined effect: in a material with an engineering grain size, the length of the deformed grain boundaries is restricted; because of that, the number of subgrains

surrounding each of those boundaries will be restricted as well.

A limitation of the analysis in this section is that it neglects the inhomogeneous distribution of the dislocation density along each deformed grain boundary. For instance, this inhomogeneity produces the subgrain-free regions surrounding the boundaries, as explained in Section 3.2. In this sense, the ρ_{GB} values employed as input to Eq. (11) are the average dislocation densities across both the subgrain-containing and subgrain-free regions surrounding each deformed grain boundary. By contrast, only the subgrain-containing areas (whose dislocation density must be higher than the boundary average) contribute to the average subgrain misorientation around the boundary. However, even with that limitation, Eq. (11) provides a good prediction of the average subgrain misorientation around the examined boundaries. Consequently, Eq. (11) constitutes a simple, physics-based method to obtain the average misorientations of the subgrains surrounding the grain boundaries of a deformed metal, as a function of the boundary dislocation density. This equation is expected to be applicable in cases where most of the dislocations around the grain boundary are forming subgrain boundaries (i.e., when significant recovery has taken place). These include deformation at high temperature and deformation of metals with a relatively high SFE, regardless of the temperature of deformation [1,2]. Moreover, the expression can be implemented in microstructural models of deformed metals to, e.g., predict the nucleation of recrystallization (which is dictated by the evolution of the subgrain misorientations from their initial values just after deformation). For cases other than those cited above, the possible validity of Eq. (11) should be assessed separately.

4. Conclusions

The substructure developed around the grain boundaries of a Ni-30% Fe austenite alloy after hot deformation to a relatively low strain (i.e., 0.2) has been systematically characterized via EBSD. These are the main findings:

1. Deformed grain boundaries are not completely surrounded by subgrains. On the contrary, considerable boundary length fractions are subgrain-free. This subgrain-free boundary length fraction decreases with higher dislocation density around the boundary. Hence, the absence of subgrains has been attributed to relatively low local dislocation densities. These retard recovery and the subsequent subgrain formation, and are in line with the low strain and high temperature applied.
2. Higher dislocation density around a boundary increases the average misorientation of the subgrains surrounding the boundary, while decreasing their average size. The decrease in the average subgrain size is suitably described by a Staker-Holt type equation. This is despite the spatial gradient and relatively high values of the dislocation densities around deformed grain boundaries, which do not exist in deformed grain interiors. In addition, a novel physics-based equation has been developed, which is able to describe the variation of the average subgrain misorientation around a boundary as a function of the average dislocation density around the boundary.
3. Subgrains at triple deformed grain junctions display considerably higher misorientations than subgrains located at other sites along deformed grain boundaries, away from the junctions. This explains the preferential nucleation of SRX at triple-junction sites, and is due to the higher dislocation densities accumulated around triple junctions. Besides, triple junctions show higher fractions of both relatively large and small subgrain sizes. The higher fraction of smaller sizes agrees with the higher dislocation densities around junctions. In turn, the higher fraction of larger sizes is due to the enhanced SIBM (bulging) at multiple grain junctions.
4. Unlike suggested by previous research, former twin boundaries (FTBs) accumulate lower dislocation densities than general HABs, at least in single-phase alloys. This leads to higher subgrain-free boundary length fractions and lower subgrain misorientations than for general HABs. Those two effects account for the lower SRX nucleation efficiencies of FTBs. Nevertheless, for the same level of dislocation density around the boundary, the developed substructure does not depend on whether the boundary is an FTB or a general HAB.

CRediT authorship contribution statement

Pablo Garcia-Chao: Writing – review & editing, Writing – original draft, Visualization, Methodology, Investigation, Formal analysis, Data curation, Conceptualization. **Winfried Kranendonk:** Writing – review & editing, Validation, Supervision. **Cornelis Bos:** Writing – review & editing, Project administration, Funding acquisition. **Jilt Sietsma:** Writing – review & editing, Funding acquisition. **Sven Erik Offerman:** Writing – review & editing, Supervision, Project administration.

Declaration of competing interest

The authors declare that they have no known competing financial interests or personal relationships that could have appeared to influence the work reported in this paper.

Acknowledgements

This work was carried out in the framework of the Research Program of the Materials Innovation Institute (M2i) (www.m2i.nl) supported by the Dutch Government [project number T17019L]. The authors wish to thank Kees Kwakernaak from TU Delft for support with experimental work. Help from Jhon Ochoa-Avendaño and Dr. Xiaohui Liang with the calculation of misorientations is also acknowledged.

Appendix A

When deriving Eq. (11), the average product $\overline{d_{SG}\theta_{SG}}$ of the diameter and misorientation of the individual subgrains neighboring a deformed grain boundary (Eq. (3)) is approximated by the product of the averages of the two variables $\overline{d}_{SG}\overline{\theta}_{SG}$. Replacing the average product of two stochastic variables by the product of their averages is valid if they are not correlated. Moreover, the average of the stochastic variables should be taken in the limit of an infinite number of observations. About the first condition, Fig. A.1 plots the diameter of the individual subgrains examined in the present study, adjacent to a deformed grain boundary, as a function of their misorientation. The correlation coefficient between the two variables is only +0.036. This confirms the absence of correlation between them. About the second condition, it is expected to be generally fulfilled, because all the subgrains adjacent to a deformed grain boundary are taken into account. Accordingly, the average error made when replacing $\overline{d_{SG}\theta_{SG}}$ by $\overline{d}_{SG}\overline{\theta}_{SG}$ for the individual deformed grain boundaries analyzed in this study (considering both general HABs and FTBs) is of ~0.2% only (average values of 27.21 and 27.27 nm for $\overline{d_{SG}\theta_{SG}}$ and $\overline{d}_{SG}\overline{\theta}_{SG}$, respectively, across all the analyzed deformed grain boundaries)

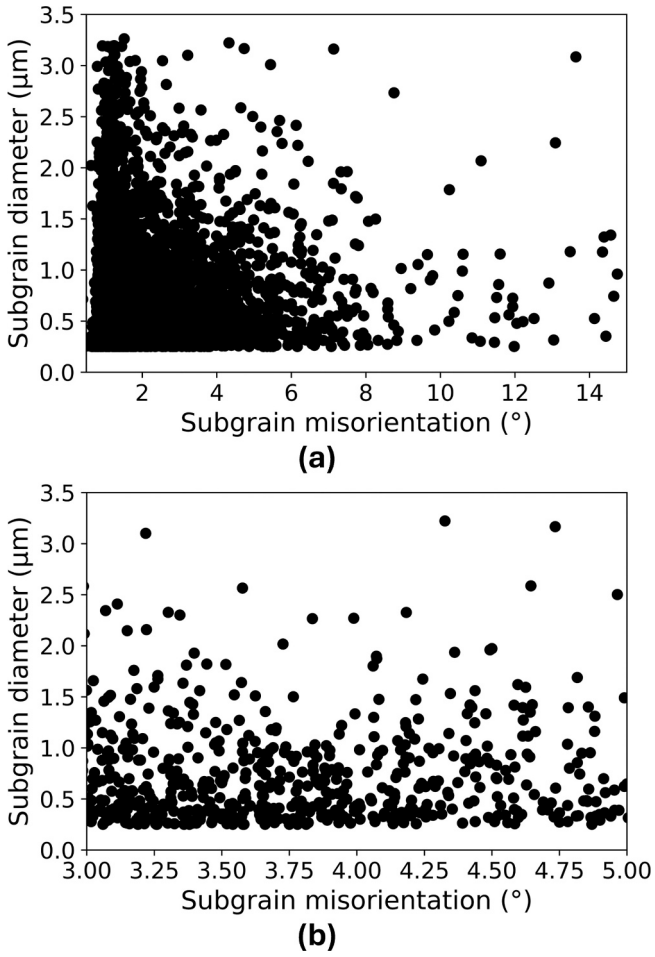

Fig. A.1. (a, b) Scatter plot representing the diameter and misorientation of all the individual subgrains observed in this study, which were adjacent to a deformed grain boundary. For clarity, (b) represents an enlarged view of (a), corresponding to a misorientation range between 3 and 5°. The correlation coefficient resulting from the scatter plot is +0.036.

Data availability

Data will be made available on request.

References

[1] T. Sakai, A. Belyakov, R. Kaibyshev, H. Miura, J.J. Jonas, Dynamic and post-dynamic recrystallization under hot, cold and severe plastic deformation conditions, Prog. Mater. Sci. 60 (2014) 130–207.
[2] A. Zelenika, A.A.W. Cretton, F. Frankus, S. Borgi, F.B. Grumsen, C. Yildirim, C. Detlefs, G. Winther, H.F. Poulsen, Observing formation and evolution of dislocation cells during plastic deformation, Sci. Rep. 15 (1) (2025) 8655.
[3] A. Rollett, G.S. Rohrer, F.J. Humphreys, Recrystallization and Related Annealing Phenomena, 3rd ed., Elsevier Health Sciences, London, 2017.
[4] D. Hull, D.J. Bacon, Introduction to Dislocations, 5th ed., Butterworth-Heinemann, London, 2011.
[5] J.G. Sevillano, P. Van Houtte, E. Aernoudt, Large strain work hardening and textures, Prog. Mater. Sci. 25 (2–4) (1980) 69–134.
[6] D.J. Lloyd, D. Kenny, The structure and properties of some heavily cold worked aluminum alloys, Acta Metall. 28 (5) (1980) 639–649.
[7] P.J. Hurley, F.J. Humphreys, The application of EBSD to the study of substructural development in a cold rolled single-phase aluminium alloy, Acta Mater. 51 (4) (2003) 1087–1102.
[8] D.A. Hughes, N. Hansen, The microstructural origin of work hardening stages, Acta Mater. 148 (2018) 374–383.
[9] C. Song, W. Shen, Z. Xie, H. Wang, R. Zhao, Z. Sun, J. Cheng, H. Yu, Developing a novel austenitic stainless steel with high yield strength and coefficient of thermal expansion, Mater. Res. Lett. 13 (9) (2025) 936–944.
[10] T. Zou, Y. Jiang, Y. Qian, T. Zhangyu, X. Gong, Z. Gao, H. Zhang, Y. Liu, Q. Wang, Physics-based multiscale investigation on the plastic deformation of AM 939 under the coupling field of temperature and strain rate, Mater. Sci. Eng. A 961 (2026) 150131.
[11] R. Sandström, Formation of cells and subgrains and its influence on properties, Metals 12 (3) (2022) 497.
[12] K. Maruyama, J. Nakamura, N. Sekido, K. Yoshimi, Causes of heat-to-heat variation of creep strength in grade 91 steel, Mater. Sci. Eng. A 696 (2017) 104–112.
[13] L. Li, Z. Zhang, P. Zhang, C. Li, Z. Zhang, Dislocation arrangements within slip bands during fatigue cracking, Mater. Charact. 145 (2018) 96–100.
[14] D. Lu, B. Lin, T. Liu, S. Deng, Y. Guo, J. Li, D. Liu, Effect of grain structure on fatigue crack propagation behavior of Al-Cu-Li alloys, J. Mater. Sci. Technol. 148 (2023) 75–89.
[15] F. Liu, Y. Chen, C. He, Y. Liu, C. Wang, Q. Wang, L. Li, Creep-fatigue voids and sub-grain boundaries assisted crack initiation for titanium alloy in VHCF regime with high mean stress at 400° C, Mater. Sci. Eng. A 844 (2022) 143171.
[16] H.S. Zurob, C.R. Hutchinson, Y. Brechet, G. Purdy, Modeling recrystallization of microalloyed austenite: effect of coupling recovery, precipitation and recrystallization, Acta Mater. 50 (12) (2002) 3077–3094.
[17] X. Du, T. Xi, C. Yang, H. Zhao, K. Yang, Cu addition retards the static recrystallization of cold-deformed 316L biomedical stainless steel, J. Mater. Res. Technol. 19 (2022) 1673–1677.
[18] T. Omori, T. Kusama, S. Kawata, I. Ohnuma, Y. Sutou, Y. Araki, K. Ishida, R. Kainuma, Abnormal grain growth induced by cyclic heat treatment, Science 341 (6153) (2013) 1500–1502.
[19] C. Yilmaz, M. Poul, L. Lahn, D. Raabe, S. Zaefferer, Dislocation-assisted particle dissolution: a new hypothesis for abnormal growth of goss grains in grain-oriented electrical steels, Acta Mater. 258 (2023) 119170.
[20] D. Juul Jensen, Y. Zhang, Nucleation of recrystallization, J. Phys. Conf. Ser. 2635 (1) (2023). IOP Publishing, p. 012001.
[21] P.J. Hurley, F.J. Humphreys, Modelling the recrystallization of single-phase aluminium, Acta Mater. 51 (13) (2003) 3779–3793.
[22] F.J. Humphreys, A unified theory of recovery, recrystallization and grain growth, based on the stability and growth of cellular microstructures—I. The basic model, Acta Mater. 45 (10) (1997) 4231–4240.
[23] M.K. Rehman, H.S. Zurob, A novel approach to model static recrystallization of austenite during hot rolling of Nb microalloyed steel. Part I: precipitate-free case, Metall. Mater. Trans. A 44 (2013) 1862–1871.

[24] H.S. Zurob, Y.J.M. Brechet, J.W.C. Dunlop, Quantitative criterion for recrystallization nucleation in single-phase alloys: prediction of critical strains and incubation times, Acta Mater. 54 (15) (2006) 3983–3990.
[25] K. Traka, E. Sepúlveda Hernández, T. Nguyen-Minh, K. Sedighiani, J. Sietsma, L.A. I. Kestens, Prediction of different recrystallisation textures under a single unified physics-based model description, Comput. Mater. Sci. 246 (2025) 113425.
[26] K. Traka, K. Sedighiani, C. Bos, J. Galan-Lopez, K. Angenendt, D. Raabe, J. Sietsma, Topological aspects responsible for recrystallization evolution in an IF-steel sheet–investigation with cellular-automaton simulations, Comput. Mater. Sci. 198 (2021) 110643.
[27] V. Shah, K. Sedighiani, J.S. Van Dokkum, C. Bos, F. Roters, M. Diehl, Coupling crystal plasticity and cellular automaton models to study meta-dynamic recrystallization during hot rolling at high strain rates, Mater. Sci. Eng. A 849 (2022) 143471.
[28] C. Haase, M. Kühbach, L.A. Barrales-Mora, S.L. Wong, F. Roters, D.A. Molodov, G. Gottstein, Recrystallization behavior of a high-manganese steel: experiments and simulations, Acta Mater. 100 (2015) 155–168.
[29] P. Garcia-Chao, W. Kranendonk, C. Bos, J. Sietsma, S.E. Offerman, The mechanism of nucleation of static recrystallization in austenite after hot deformation, Mater. Des. 262 (2026) 115421.
[30] H. Zhu, Y. Zou, Q. Gao, Y. Tang, J. Cheng, H. Ding, Achieving a high elongation of 1700% at low temperatures in a cold-rolled Fe-24Mn-10Al-1C lightweight steel, Mater. Res. Lett. (2026) 1–9.
[31] X. Huang, S. Guo, W. Chen, Effect of initial grain size on dynamic recrystallization of ultra-large nuclear rotor steel 25Cr2Ni4MoV, Materialia 39 (2025) 102362.
[32] N. Cliche, D. Piot, S. Ringeval, F. Cortial, J.-L. Heuzé, C. Desrayaud, A.-F. Gourgues-Lorenzon, High-temperature flow behavior and associated microstructural evolution of 316Nb austenitic stainless steel-transition between discontinuous and continuous dynamic recrystallization, Mater. Sci. Eng. A 948 (2025) 149249.
[33] Z. Xie, C. Song, W. Shen, H. Wang, Z. Sun, H. Yu, J. Cheng, First-principles study on the effect of Ce on segregation behavior of bcc-Fe grain boundaries in low-carbon low-alloy steel, J. Mater. Res. Technol. 36 (2025) 10474–10486.
[34] A.S. Taylor, P. Cizek, P.D. Hodgson, Comparison of 304 stainless steel and Ni–30 wt.% Fe as potential model alloys to study the behaviour of austenite during thermomechanical processing, Acta Mater. 59 (14) (2011) 5832–5844.
[35] A.S. Taylor, P. Cizek, P.D. Hodgson, Orientation dependence of the substructure characteristics in a Ni–30Fe austenitic model alloy deformed in hot plane strain compression, Acta Mater. 60 (4) (2012) 1548–1569.
[36] P.J. Hurley, F.J. Humphreys, Characterizing the deformed state in Al-0.1 Mg alloy using high-resolution electron backscattered diffraction, J. Microsc. 205 (3) (2002) 218–225.
[37] M.R. Staker, D.L. Holt, The dislocation cell size and dislocation density in copper deformed at temperatures between 25 and 700 C, Acta Metall. 20 (4) (1972) 569–579.
[38] P. Faivre, R.D. Doherty, Nucleation of recrystallization in compressed aluminium: studies by electron microscopy and Kikuchi diffraction, J. Mater. Sci. 14 (1979) 897–919.
[39] N. Haghdadi, P. Cizek, H. Beladi, P.D. Hodgson, A novel high-strain-rate ferrite dynamic softening mechanism facilitated by the interphase in the austenite/ferrite microstructure, Acta Mater. 126 (2017) 44–57.
[40] A. Godfrey, D. Hughes, Scaling of the spacing of deformation induced dislocation boundaries, Acta Mater. 48 (8) (2000) 1897–1905.
[41] H. Beladi, P. Cizek, P.D. Hodgson, Dynamic recrystallization of austenite in Ni-30 Pct Fe model alloy: microstructure and texture evolution, Metall. Mater. Trans. A 40 (2009) 1175–1189.
[42] M. Kubota, K. Ushioda, G. Miyamoto, T. Furuhara, Analysis of recrystallization behavior of hot-deformed austenite reconstructed from electron backscattering diffraction orientation maps of lath martensite, Scr. Mater. 112 (2016) 92–95.
[43] P. Garcia-Chao, J.J. Eipe, M. Krugla, C. Bos, J. Sietsma, W. Kranendonk, S. E. Offerman, Nucleation sites in the static recrystallization of a hot-deformed Ni-30 Pct Fe austenite model alloy, Metall. Mater. Trans. A 54 (6) (2023) 2160–2177.
[44] Q. He, S. Xia, Q. Bai, Y. Zhang, L. Li, The recrystallization nucleation mechanism for a low-level strained 316L stainless steel and its implication to twin-induced grain boundary engineering, Metall. Mater. Trans. A 55 (11) (2024) 4525–4542.
[45] S.I. Wright, M.M. Nowell, R. De Kloe, L. Chan, Orientation precision of electron backscatter diffraction measurements near grain boundaries, Microsc. Microanal. 20 (3) (2014) 852–863.
[46] J. Jiang, T.B. Britton, A.J. Wilkinson, Evolution of dislocation density distributions in copper during tensile deformation, Acta Mater. 61 (19) (2013) 7227–7239.
[47] S. Zhang, W. Liu, J. Wan, R.D.K. Misra, Q. Wang, C. Wang, The grain size and orientation dependence of geometrically necessary dislocations in polycrystalline aluminum during monotonic deformation: relationship to mechanical behavior, Mater. Sci. Eng. A 775 (2020) 138939.
[48] J.E. Bailey, P.B. Hirsch, The recrystallization process in some polycrystalline metals, Proc. R. Soc. Lond. A Math. Phys. Sci. 267 (1328) (1962) 11–30.
[49] A.M. Wusatowska-Sarnek, H. Miura, T. Sakai, Nucleation and microtexture development under dynamic recrystallization of copper, Mater. Sci. Eng. A 323 (1–2) (2002) 177–186.
[50] D. Ponge, G. Gottstein, Necklace formation during dynamic recrystallization: mechanisms and impact on flow behavior, Acta Mater. 46 (1) (1998) 69–80.
[51] P. Garcia-Chao, W. Kranendonk, C. Bos, J. Sietsma, S.E. Offerman, Substructure Development and the Nucleation Mechanism of Static Recrystallization in Austenite after Hot Deformation, 2026. Available at SSRN 5180529.
[52] H. Beladi, P. Cizek, A.S. Taylor, G.S. Rohrer, P.D. Hodgson, Static softening in a Ni-30Fe austenitic model alloy after hot deformation: microstructure and texture evolution, Metall. Mater. Trans. A 48 (2017) 855–867.
[53] Z. Aretxabaleta, B. Pereda, B. López, Analysis of the effect of Al on the static softening kinetics of C-Mn steels using a physically based model, Metall. Mater. Trans. A 45 (2014) 934–947.
[54] A. Laasraoui, J.J. Jonas, Recrystallization of austenite after deformation at high temperatures and strain rates—analysis and modeling, Metall. Trans. A. 22 (1991) 151–160.
[55] H. Mughrabi, Implications of non-negligible microstructural variations during steady-state deformation, Int. J. Mater. Res. 96 (6) (2022) 546–551.
[56] N.A. Koneva, V.A. Starenchenko, D.V. Lychagin, L.I. Trishkina, N.A. Popova, E. V. Kozlov, Formation of dislocation cell substructure in face-centred cubic metallic solid solutions, Mater. Sci. Eng. A 483 (2008) 179–183.
[57] M. Xu, Q. Xiao, X. Zu, Y. Tan, Z. Huang, Constitutive Modeling of annealed OFHC with wide strain-rate and temperature effects: incorporating dislocation dynamics and normalized microstructural size evolution, Materials 16 (19) (2023) 6517.
[58] A. Turnali, A. Hariharan, E. Polatidis, N.J. Peter, J. Gehlmann, C. Sofras, Z. Hegedüs, L. Sayk, T. Allam, J.H. Schleifenbaum, Harnessing additive manufacturing-induced microstructure and solute heterogeneities for the design of precipitation-strengthened alloys, Acta Mater. 298 (2025) 121423.
[59] J.J. Bhattacharyya, S. Faberman, A. Sullivan, M. Saha, T. Sasaki, S.R. Agnew, Strain partitioning-induced anisotropy in thermomechanically processed magnesium alloys comprised of earth-abundant elements, Scr. Mater. 262 (2025) 116659.
[60] L. Chen, C. Liu, P. Ma, J. Yang, L. Zhan, M. Huang, Strong in-plane anisotropy of creep ageing behavior in largely pre-deformed Al-Cu alloy: experiments and constitutive modeling, Int. J. Plast. 152 (2022) 103245.
[61] L. Cui, S. Jiang, J. Xu, R.L. Peng, R.T. Mousavian, J. Moverare, Revealing relationships between microstructure and hardening nature of additively manufactured 316L stainless steel, Mater. Des. 198 (2021) 109385.
[62] N. Kumar, R.S. Mishra, C. Huskamp, K.K. Sankaran, Critical grain size for change in deformation behavior in ultrafine grained Al–Mg–Sc alloy, Scr. Mater. 64 (6) (2011) 576–579.
[63] S.S. Hansen, J.B. Vander Sande, M. Cohen, Niobium carbonitride precipitation and austenite recrystallization in hot-rolled microalloyed steels, Metall. Trans. A. 11 (1980) 387–402.
[64] B. Xie, H. Li, Y. Ning, M. Fu, Discontinuous dynamic recrystallization and nucleation mechanisms associated with 2-, 3-and 4-grain junctions of polycrystalline nickel-based superalloys, Mater. Des. 231 (2023) 112041.
[65] J.C. Stinville, N. Vanderesse, F. Bridier, P. Bocher, T.M. Pollock, High resolution mapping of strain localization near twin boundaries in a nickel-based superalloy, Acta Mater. 98 (2015) 29–42.
[66] S.R. Yeratapally, M.G. Glavicic, M. Hardy, M.D. Sangid, Microstructure based fatigue life prediction framework for polycrystalline nickel-base superalloys with emphasis on the role played by twin boundaries in crack initiation, Acta Mater. 107 (2016) 152–167.
[67] J.C. Stinville, E.R. Yao, P.G. Callahan, J. Shin, F. Wang, M.P. Echlin, T.M. Pollock, D.S. Gianola, Dislocation dynamics in a nickel-based superalloy via in-situ transmission scanning electron microscopy, Acta Mater. 168 (2019) 152–166.
[68] T.R. Bieler, P. Eisenlohr, F. Roters, D. Kumar, D.E. Mason, M.A. Crimp, D. Raabe, The role of heterogeneous deformation on damage nucleation at grain boundaries in single phase metals, Int. J. Plast. 25 (9) (2009) 1655–1683.
[69] X. Zhang, J.-C. Stinville, T.M. Pollock, F.P.E. Dunne, Crystallography and elastic anisotropy in fatigue crack nucleation at nickel alloy twin boundaries, J. Mech. Phys. Solids 155 (2021) 104538.
[70] J. Genée, L. Signor, P. Villechaise, Slip transfer across grain/twin boundaries in polycrystalline Ni-based superalloys, Mater. Sci. Eng. A 701 (2017) 24–33.
[71] A. Smith, S.E. Kruger, J. Sietsma, S. van Der Zwaag, Laser-ultrasonic monitoring of austenite recrystallization in C–Mn steel, ISIJ Int. 46 (8) (2006) 1223–1232.
[72] O. Kwon, A.J. DeArdo, Interactions between recrystallization and precipitation in hot-deformed microalloyed steels, Acta Metall. Mater. 39 (4) (1991) 529–538.
[73] H. Beladi, P. Cizek, P.D. Hodgson, On the characteristics of substructure development through dynamic recrystallization, Acta Mater. 58 (9) (2010) 3531–3541.
[74] W. Pantleon, N. Hansen, Dislocation boundaries—the distribution function of disorientation angles, Acta Mater. 49 (8) (2001) 1479–1493.
[75] F.J. Humphreys, Review grain and subgrain characterisation by electron backscatter diffraction, J. Mater. Sci. 36 (2001) 3833–3854.
[76] W. Charnock, J. Nutting, The effect of carbon and nickel upon the stacking-fault energy of iron, Met. Sci. J. 1 (1) (1967) 123–127.
[77] Y. Adachi, M. Wakita, H. Beladi, P.D. Hodgson, The formation of ultrafine ferrite through static transformation in low carbon steels, Acta Mater. 55 (14) (2007) 4925–4934.
[78] H. Beladi, P. Cizek, P.D. Hodgson, New insight into the mechanism of metadynamic softening in austenite, Acta Mater. 59 (4) (2011) 1482–1492.
[79] W. Chen, C. Jia, B. Hu, C. Zheng, D. Li, Evolution of twins and sub-boundaries at the early stage of dynamic recrystallization in a Ni-30% Fe austenitic model alloy, Mater. Sci. Eng. A 733 (2018) 419–428.
[80] P. Mannan, G. Casillas, E.V. Pereloma, The effect of Nb solute and NbC precipitates on dynamic and metadynamic recrystallisation in Ni-30Fe-Nb-C model alloys, Mater. Sci. Eng. A 700 (2017) 116–131.
[81] R.H. Petrov, L.A.I. Kestens, Advanced high-strength steels: electron backscatter diffraction (EBSD), in: Encyclopedia of Iron, Steel, and their Alloys, Taylor & Francis, Boca Raton (FL), 2016.

[82] F.J. Humphreys, P.S. Bate, P.J. Hurley, Orientation averaging of electron backscattered diffraction data, J. Microsc. 201 (1) (2001) 50–58.
[83] S.I. Wright, M.M. Nowell, S.P. Lindeman, P.P. Camus, M. De Graef, M.A. Jackson, Introduction and comparison of new EBSD post-processing methodologies, Ultramicroscopy 159 (2015) 81–94.
[84] P. Garcia-Chao, T. Nyyssönen, A. Ståhlkrantz, H. Magnusson, Annealing twin development in austenite in steels after hot deformation, Mater. Charact. 224 (11501) (2025) 2.
[85] D.P. Field, P.B. Trivedi, S.I. Wright, M. Kumar, Analysis of local orientation gradients in deformed single crystals, Ultramicroscopy 103 (1) (2005) 33–39.
[86] R.J. Wakelin, E.L. Yates, A study of the order-disorder transformation in Iron-nickel alloys in the region FeNi3, Proc. Phys. Soc. Sect. B. 66 (3) (1953) 221.
[87] B. Larrouy, P. Villechaise, J. Cormier, O. Berteaux, Grain boundary–slip bands interactions: impact on the fatigue crack initiation in a polycrystalline forged Ni-based superalloy, Acta Mater. 99 (2015) 325–336.
[88] A. Kundu, D.P. Field, Influence of plastic deformation heterogeneity on development of geometrically necessary dislocation density in dual phase steel, Mater. Sci. Eng. A 667 (2016) 435–443.
[89] T.J. Ruggles, T.M. Rampton, A. Khosravani, D.T. Fullwood, The effect of length scale on the determination of geometrically necessary dislocations via EBSD continuum dislocation microscopy, Ultramicroscopy 164 (2016) 1–10.
[90] J. Jiang, T.B. Britton, A.J. Wilkinson, Measurement of geometrically necessary dislocation density with high resolution electron backscatter diffraction: effects of detector binning and step size, Ultramicroscopy 125 (2013) 1–9.
[91] Q. Liu, N. Hansen, Geometrically necessary boundaries and incidental dislocation boundaries formed during cold deformation, Scr. Metall. Mater. 32 (8) (1995).